This article has been accepted for publication in a future issue of this journal, but has not been fully edited. Content may change prior to final publication. Citation information: DOI 10.1109/TPWRS.2021.3061434, IEEE Transactions on Power Systems

Understanding Small-Signal Stability of Low-Inertia Systems

Uros Markovic, *Member, IEEE,* Ognjen Stanojev, *Student Member, IEEE,* Petros Aristidou, *Senior Member, IEEE,* Evangelos Vrettos, *Member, IEEE,* Duncan Callaway, *Senior Member, IEEE,* Gabriela Hug, *Senior Member, IEEE*

***Abstract*—Large-scale integration of renewable generation, usually interfaced to the network through power electronics, has led to drastic changes in power system dynamics. This paper presents novel insights into stability properties of such systems. For that purpose, a high-fidelity dynamic model of a generic low-inertia power system has been developed. The full-order, state-of-the-art control schemes of both synchronous and converter-based generators are included, with the latter differentiating between *grid-forming* and *grid-following* mode of operation. Furthermore, the dynamics of transmission lines and loads are captured in the model. Using modal analysis techniques such as participation factors and parameter sensitivity, the most vulnerable segments of the system are determined and the adverse effects of timescale coupling and control interference are investigated. More precisely, this work characterizes the maximum permissible penetration levels of inverter-based generation as well as the nature of the associated unstable modes and the underlying dynamics. Finally, potential directions for improving the system stability margin under different generation portfolios are proposed for several benchmark systems.**

***Index Terms*—differential-algebraic equations, voltage source converter, synchronous generator, small-signal stability, low-inertia systems**

I. Introduction

Due to convergence of economic and policy drivers, large-scale electric power grids are hosting rapidly increasing amounts of wind and solar generation as well as battery storage. These sources often interface with the grid via Voltage Source Converters (VSCs), whose interaction with the grid is substantially different from synchronous machines and poses many challenges for power system modeling, analysis and control [1]. Moreover, a high penetration of fast-acting VSCs may create unexpected couplings and existing control approaches may become less valid, thus adversely affecting frequency and voltage stability. With the aim of providing solutions to the underlying problems, detailed and accurate models of low-inertia systems in the form of Ordinary Differential Equation (ODE) are needed for the purpose of small-signal analysis.

The field of small-signal analysis is well established for conventional power systems [2]–[4]. With the increasing integration of renewables, a number of publications addressing modeling and stability of $100\,\%$ inverter-based microgrids has emerged, varying from the analysis of individual converter operation modes in a single-machine infinite-bus equivalent [5]–[10] to operation of small and real-size distribution grids [11]–[21]. The former studies mostly emphasize the validation of the proposed small-signal models and provide insights into the stability characteristics and modes of individual inverter control schemes by analyzing their sensitivities with respect to system parameters. In particular, [5] and [6] investigate stability properties of *grid-supporting* inverters operating as virtual synchronous machines, [7] compares dynamic characteristics of droop-based *grid-feeding* and *grid-supporting* VSCs, whereas [8]–[10] extend these analyses to different types of *grid-forming* and *grid-following* converter control schemes. While providing valuable insights into the operation of individual converter-interfaced generation units, all aforementioned studies consider single-generator models and a stiff grid equivalent, which oversimplifies the problem.

Multi-inverter configurations have also been thoroughly investigated in the literature. Studies in [11]–[13] propose various state-space models for small systems comprised of two or three inverters connected through constant impedance lines, followed by stability analyses such as droop gain parameter sweeps and the impact of R/X ratio of the interconnecting cables. However, the authors use simplified inverter models comprising only droop control and LCL filter dynamics, thus neglecting device-level control and line dynamics in the process. Moreover, they only consider *grid-forming* operation and do not take into account a potentially adverse impact of Phase-Locked Loops (PLLs) on system stability. Alternatively, [14] focuses on interactions between a virtual synchronous generator and a converter-interfaced load by considering small-signal stability under different operating conditions. While the authors include a dynamic model of the load and the interconnecting line, they analyze stability solely via parameter sweeps of the virtual inertia constant and load impedance, which does not provide enough insight into the nature of potential instabilities. A more general and rigorous approach towards synchronization and stability analysis of droop-based microgrids is taken in [15]–[17], where the appropriate conditions for synchronization, power sharing and voltage stability of droop-controlled inverters in islanded microgrids have been derived. Nevertheless, the aforementioned simplifications in terms of model complexity are still present.

In contrast, the studies in [19]–[22] focus on detailed system models which include both low and high inverter frequency dynamics as well as the network and load dynamics, and propose accurate small-signal representation of real-size microgrids. The work in [22] provides analysis in terms of system eigenvalues and their sensitivity to different states. It was observed that the dominant low-frequency modes are highly sensitive to network configuration and the parameters of the power sharing controller, whereas the high frequency modes are largely sensitive to the inverter inner loop controllers, network dynamics, and load dynamics. However, only grid-forming mode of operation has been taken into consideration. Alternatively, the authors in [19] present a new methodology for forming, augmenting, and modifying the state-space matrices of large microgrids comprising both grid-forming and grid-following inverter control schemes, and investigate a $100\,\%$ inverter-based 69-bus distribution system. The emphasis is however on model validation, state matrix partitioning and optimal control tuning for improving the oscillatory modes in the system, but not on the stability analysis. Furthermore, [20] sets a particular focus on inner cascade loops and the differences in small-signal stability of a three-inverter microgrid

0885-8950 (c) 2021 IEEE. Personal use is permitted, but republication/redistribution requires IEEE permission. See http://www.ieee.org/publications_standards/publications/rights/index.html for more information.
Authorized licensed use limited to: Cyprus University of Technology. Downloaded on March 18,2021 at 09:27:38 UTC from IEEE Xplore. Restrictions apply.

This article has been accepted for publication in a future issue of this journal, but has not been fully edited. Content may change prior to final publication. Citation information: DOI 10.1109/TPWRS.2021.3061434, IEEE Transactions on Power Systems

utilizing conventional PI-based and internal model-based control approaches. Eigenvalue sensitivity analysis with respect to power droop gains and filter inductance again reveals that the low-frequency modes are highly sensitive to the parameters of the power sharing controllers for both methods.

On the other hand, [21] proposes an approximation method based on critical clusters for assessing the droop gain stability margins of medium-scale islanded microgrids that takes advantage of the fact that the contribution of inverters to the small-signal stability may depend on their location and the interactions with each other. Both [20] and [21] are however solely restricted to grid-forming VSCs and do not investigate the adverse interactions between different converter control schemes. The latter aspect is partially tackled in [23] by analyzing stability issues between a grid-feeding VSC and an inverter operating as a virtual synchronous generator, with a focus on virtual inertia characteristics and interaction between power converters and the AC grid. Moreover, [23]–[25] highlight some conceptual differences between a traditional and an inverter-based power system in terms of associated control timescales. Nonetheless, they all confine the analysis only to $100\,\%$ inverter-based microgrids.

While the aforementioned studies provide various perspectives on stability of microgrids and zero-inertia systems, less emphasis has been placed on performance of large-scale systems with a mixture of synchronous machines and VSCs. Having in mind that operators in Ireland [26], Texas [27] and South Australia [28] are already facing obstacles regarding high wind penetration during certain periods of the day, the fundamental understanding of low-inertia systems and their stability properties is of crucial importance. Nevertheless, simulation and analysis of large power systems with a mix of synchronous and converter-based generation involves a significant computational burden. To this end, commercial software packages such as PSLF [29], DSATools [30] and PSS/E [31] are widely employed, both for industrial and academic purposes. While these software tools incorporate detailed dynamic models of different generator types and provide means for large-scale time-domain simulations, they are restricted in terms of analytical capabilities and flexibility. This mostly stems from underlying modeling assumptions valid for traditional Synchronous Generator (SG)-based power networks, which are not applicable to inverter-dominated systems. For instance, the widely employed dynamic models for wind and photovoltaic plants, originally proposed by WECC renewable energy modeling task force [32], do not consider dynamics of high-frequency converter controls and PLLs, which can have a detrimental impact on stability. Furthermore, transmission line dynamics are typically neglected in power system studies due to drastically shorter timescales compared to SG dynamics. With the introduction of fast-acting Power Electronic (PE) devices, such assumptions are not valid anymore [1].

In turn, the existing literature on stability of large-scale transmission systems with high share of inverter-based generation tends to neglect important aspects of system dynamics and confine the analytical analysis to simplified mathematical models and state-space formulations. More precisely, [33]–[36] study the impact of large-scale wind power generation on power system oscillation, transient and small-signal stability. However, the authors either use oversimplified synchronous generator models (i.e., not equipped with governors and exciters) [33], neglect inner control loops of inverter-interfaced wind generation [34], [35] or focus on high-level probabilistic frameworks [36], which obstructs them from capturing some important dynamic interactions and phenomena. On the other hand, [37] and [38] employ systematic nonlinear simulations and off-the-shelf small-signal analysis tools to assess the impact of increased penetration of wind and photovoltaic generation on stability of the Kundur two-area and the western North American power system, respectively. Both studies are however restricted solely to the investigation of inter-area oscillations and the nature of underlying oscillatory modes.

Alternatively, a two-bus system comprising a *grid-following* VSC and a synchronous generator was investigated in [39] and [40] through eigenvalue analysis. Both studies point out that the PLL can be a source of oscillatory modes and instability. The work in [39] incorporates relatively detailed control structures of both units, but mostly focuses on model validation and sensitivity analysis to determine the optimal ranges of relevant control parameters. On the other hand, the authors in [40] provide insightful remarks regarding the permissible penetration levels of *grid-following* inverters, as well as the relevance of different controllers on small-signal stability. However, they employ an inverter scaling method that complicates model implementation on a larger system and omit the Power System Stabilizer (PSS) and important flux dynamics from the SG model. Furthermore, neither of the aforementioned studies explore the deeper causes of instability, nor consider the impact of different converter operation modes. Finally, the focus is primarily on distribution networks and microgrids, thus neglecting the potential impact of transmission line dynamics.

The work presented in this paper improves on the existing literature in several ways. In contrast to [19]–[25], we include several converter operation modes and investigate their interactions in a $100\,\%$ inverter-dominated transmission network. The analysis is also extended to low-inertia systems and the adverse interference between different components of synchronous and converter-based generation. However, unlike the work in [33]–[40], we employ a more detailed representation of a generic, low-inertia system that captures all relevant physical properties and associated dynamics, including various generation models and control schemes as well as line and load dynamics. Moreover, unlike most of the existing studies, we are not primarily concerned with parameter sensitivity but rather with investigating maximum permissible penetrations of PE-interfaced generation under various system configurations. In particular, the critical levels of installed inverter-based generation and the key modes of arising instability are identified and mapped back to the respective controller dynamics.

Our findings suggest that the root cause of instability cannot be associated solely with the aggregate power injection of VSC units, as it varies depending on the installed capacity and operating setpoints of renewable generation. Additionally, the problems arising from underlying timescale coupling of converter and transmission line dynamics, as well as the timescale separation between the respective VSC and SG controllers regulating the same system quantities have been observed. As a result, new insights into the overall stability of low- and no-inertia systems are presented, together with potential directions for improving the system stability margin under different generation portfolios and the analytical expressions for necessary control criteria pertaining to the impact of line dynamics. Furthermore, some of the widely common premises in terms of stability and overall system dynamics have been debunked solely as an artifact of inadequate modeling and system representation, which justifies the importance of the proposed ODE formulation and the level

0885-8950 (c) 2021 IEEE. Personal use is permitted, but republication/redistribution requires IEEE permission. See http://www.ieee.org/publications_standards/publications/rights/index.html for more information.
Authorized licensed use limited to: Cyprus University of Technology. Downloaded on March 18,2021 at 09:27:38 UTC from IEEE Xplore. Restrictions apply.

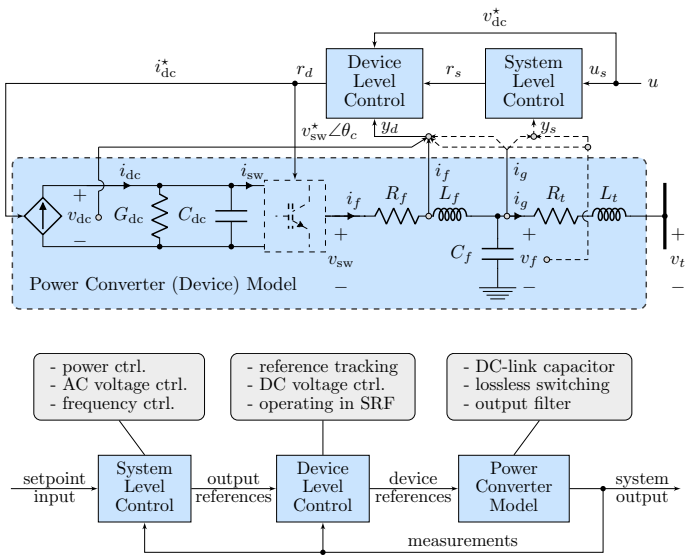

Fig. 1. Representation of the VSC model: two-level VSC connected through a transformer to the grid (top); general input-output block structure of the power converter model and its control scheme (bottom).

of detail included in this study.

The remainder of the paper is structured as follows. In Section II, detailed dynamical models and control schemes of synchronous and converter-based generators are presented, together with the general ODE formulation of an arbitrary low-inertia power system. Subsequently, the underlying timescales and the potential adverse dynamical interactions are discussed in Section III. The numerical results from different case studies and the respective small-signal stability margins are illustrated in Sections IV and V, whereas Section VI draws the main conclusions and discusses the key findings and outlook of the study.

II. Power System Modeling

The proposed model includes detailed representation of relevant dynamics and controls pertaining to synchronous and converter-interfaced generation, with the latter one encompassing both *grid-forming* and *grid-following* mode of operation. In addition, the dynamics of network elements such as impedance loads, shunt capacitors and transmission lines are also taken into consideration.

We use $\mathbb{R}$ to denote the set of real and natural numbers and, e.g., $\mathbb{R}_{\geq a} \coloneqq \{x \in \mathbb{R} | x \geq a\}$. Given an angle $\theta \in [-\pi, \pi)$, the 2-D rotation matrix is given by

$$\mathcal{R}(\theta) \coloneqq \begin{bmatrix} \cos\theta & -\sin\theta \\ \sin\theta & \cos\theta \end{bmatrix} \in \mathbb{R}^{2\times 2}. \tag{1}$$

Moreover, we define the $90°$ rotation matrix $j \coloneqq \mathcal{R}(\pi/2)$ that can be interpreted as an embedding of the complex imaginary unit $\sqrt{-1}$ into $\mathbb{R}^2$. For column vectors $x \in \mathbb{R}^n$ and $y \in \mathbb{R}^m$ we use $(x, y) = [x^\mathsf{T}, y^\mathsf{T}]^\mathsf{T} \in \mathbb{R}^{n+m}$ to denote a stacked vector. Furthermore, I_n denotes the identity matrix of dimension n, $\otimes$ denotes the Kronecker product, and $\|x\|$ denotes the Euclidean norm. Matrices of zeros of dimension $n \times m$ are denoted by $\mathbb{0}_{n\times m}$, and $\mathbb{0}_n$ and $\mathbb{1}_n$ denote column vectors of zeros and ones of length n.

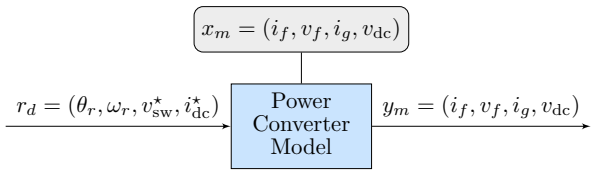

Fig. 2. Simplified MIMO structure of the device model.

A. Converter Control Scheme

The prevalent control architecture for power converters is the two-level VSC shown in Fig. 1. In this setup, an outer *system-level* control provides a reference for the converter's terminal voltage that is subsequently tracked by a cascaded *device-level* controller. We first present the model of a two-level voltage source converter and subsequently discuss the individual control blocks depicted in Fig. 1.

1) Power Converter Model: The three-phase power converter model (i.e., the device model in Fig. 1) used in this study consists of a DC-link capacitor, a lossless switching block which modulates the DC-capacitor voltage $v_{\mathrm{dc}} \in \mathbb{R}_{>0}$ into a three-phase AC voltage $v_{\mathrm{sw}}^{abc} \in \mathbb{R}^3$, and an output filter. Throughout this work, we assume that the DC-source current $i_{\mathrm{dc}} \in \mathbb{R}_{>0}$ is supplied by a controllable source (e.g., an energy storage or a curtailed renewable generation) and can be used as a control input. Averaging the dynamics over one switching period and expressing them in per-unit yields:

$$\frac{c_{\mathrm{dc}}}{\omega_b}\dot{v}_{\mathrm{dc}} = -g_{\mathrm{dc}} v_{\mathrm{dc}} - i_{\mathrm{sw}} + i_{\mathrm{dc}}, \tag{2a}$$

$$\frac{\ell_f}{\omega_b}\dot{i}_f^{abc} = -r_f i_f^{abc} + v_{\mathrm{sw}}^{abc} - v_f^{abc}, \tag{2b}$$

$$\frac{c_f}{\omega_b}\dot{v}_f^{abc} = +i_f^{abc} - i_g^{abc}, \tag{2c}$$

where $c_{\mathrm{dc}} \in \mathbb{R}_{>0}$ and $g_{\mathrm{dc}} \in \mathbb{R}_{>0}$ denote the DC capacitance and conductance, and $c_f \in \mathbb{R}_{>0}$, $\ell_f \in \mathbb{R}_{>0}$, $r_f \in \mathbb{R}_{>0}$ represent the AC filter capacitance, inductance and resistance, respectively. The converter is controlled by the modulation signal $m^{abc} \in [-\mathbb{1}_3, \mathbb{1}_3]$ that controls the modulated three-phase voltage $v_{\mathrm{sw}}^{abc} = \frac{1}{2} m^{abc} v_{\mathrm{dc}}$ and the current $i_{\mathrm{sw}} = \frac{1}{2} m^{abc\mathsf{T}} i_f^{abc}$ flowing into the switching block. Moreover, we use $i_f^{abc} \in \mathbb{R}^3$, $v_f^{abc} \in \mathbb{R}^3$, and $i_g^{abc} \in \mathbb{R}^3$ to denote the three-phase filter current, three-phase converter voltage and three-phase current injection into the system. As this work deals strictly with per-unit formulation of converter models and controls, the explicit per-unit declaration of system variables in (2) and the rest of the paper will be omitted for brevity.

We assume that the three-phase signals are balanced and, given a reference angle $\theta_r \in [-\pi, \pi)$, the converter variables can be defined in a rotating dq-reference frame by applying the power-variant dq-transform (see e.g., [41])

$$T(\theta_r) \coloneqq \frac{2}{3}\begin{bmatrix} \cos\theta_r & \cos(\theta_r - \frac{2\pi}{3}) & \cos(\theta_r + \frac{2\pi}{3}) \\ \sin\theta_r & \sin(\theta_r - \frac{2\pi}{3}) & \sin(\theta_r + \frac{2\pi}{3}) \end{bmatrix} \tag{3}$$

to the three-phase converter signals (e.g., $v_f^{dq} = T(\theta_r) v_f^{abc}$). For reasons similar to the ones pertaining to per-unit notation, the dq superscript will not be used in the remainder of the paper, i.e., the presented converter model will be described in dq-vector form $x \coloneqq x^{dq} \coloneqq (x^d, x^q)$ and per-unit. Therefore, guided

0885-8950 (c) 2021 IEEE. Personal use is permitted, but republication/redistribution requires IEEE permission. See http://www.ieee.org/publications_standards/publications/rights/index.html for more information.
Authorized licensed use limited to: Cyprus University of Technology. Downloaded on March 18,2021 at 09:27:38 UTC from IEEE Xplore. Restrictions apply.

This article has been accepted for publication in a future issue of this journal, but has not been fully edited. Content may change prior to final publication. Citation information: DOI 10.1109/TPWRS.2021.3061434, IEEE Transactions on Power Systems

by the practice commonly employed in power electronics (see Appendix A), we rewrite filter dynamics in (2b)-(2c) as

$$\dot{i}_f = \frac{\omega_b}{\ell_f}(v_{\rm sw} - v_f) - \left(\frac{r_f}{\ell_f}\omega_b + j\omega_b\omega_r\right) i_f, \tag{4a}$$

$$\dot{v}_f = \frac{\omega_b}{c_f}(i_f - i_g) - j\omega_b\omega_r v_f. \tag{4b}$$

The converter is usually interfaced to the grid through a transformer, with the dynamics of transformer current (i.e., current injected into the grid) described by

$$\dot{i}_g = \frac{\omega_b}{\ell_t}(v_f - v_t) - \left(\frac{r_t}{\ell_t}\omega_b + j\omega_b\omega_r\right) i_g, \tag{4c}$$

where $r_t \in \mathbb{R}_{>0}$ and $\ell_t \in \mathbb{R}_{>0}$ denote the transformer's per-unit resistance and inductance, $v_t \in \mathbb{R}^2$ is the voltage at the connection terminal, and $\omega_r \in \mathbb{R}_{>0}$ is the normalized reference for the angular velocity of the dq-frame.

Expressions in (4) represent the AC-side dynamics of the power converter and, together with DC-side dynamics in (2a), complete the $7^{\rm th}$-order power converter model described by $x_m = (i_f, v_f, i_g, v_{\rm dc}) \in \mathbb{R}^7$ and depicted in Fig. 2. The input vector comprises device-level references[1] $r_d = (\theta_r, \omega_r, v^\star_{\rm sw}, i^\star_{\rm dc}) \in \mathbb{R}^5$ and the measurement output y_m encompasses full state feedback for system- and device-level control (i.e., $x_m \subset y_m$), as well as the converter's AC-voltage magnitude $V_c \in \mathbb{R}_{>0}$ and instantaneous active and reactive power injection $(p_c, q_c) \in \mathbb{R}^2$ given by

$$V_c \coloneqq \|v_f\|, \quad p_c \coloneqq v_f^{\mathsf{T}} i_g, \quad q_c \coloneqq v_f^{\mathsf{T}} j^{\mathsf{T}} i_g. \tag{5}$$

The latter three measurements are directly obtained from converter's output voltage v_f and current i_g and are therefore not explicitly included in $y_m \coloneqq x_m$ for brevity. However, these measurements will be considered available to the system-level control. In fact, this control layer often includes processing of v_f and i_g such that the quantities in (5) are internally obtained. Moreover, note that we assume $v_{\rm sw} \coloneqq v^\star_{\rm sw}$, i.e., the modulation voltage reference $v^\star_{\rm sw}$ is perfectly transformed to the AC side. Due to high modeling complexity and very fast underlying dynamics [42], the converter switching is not included in the model nor will it be considered throughout this study.

2) System-Level Control: The desired dynamic behavior of the power converter as seen from the system point of view is commonly prescribed by a dynamic controller of the form

$$\dot{x}_s = \kappa(x_s, y_s, u_s), \tag{6a}$$

$$r_s = h(x_s, y_s, u_s), \tag{6b}$$

where $x_s \in \mathbb{R}^n$ is a vector of internal controller states, $y_s \in \mathbb{R}^m$ are the measured converter outputs, $u_s \in \mathbb{R}^p$ are the prescribed control setpoints, and $r_s \in \mathbb{R}^q$ is a vector of computed references sent to the device-level control. A simplified representation of the general MIMO structure for both *grid-forming* and *grid-following* operation mode is illustrated in Fig. 3, with the former mode potentially differentiating between several representative classes of control such as droop control [43], [44], Virtual Synchronous Machine (VSM) control [45], [46], Virtual Oscillator Control (VOC) [47], [48] and matching control [49], [50]. However, under certain trivial conditions, all aforementioned control strategies showcase a small-signal equivalence (see e.g., [48]), and can be subsumed under a single droop-based controller

[1]We assume perfect tracking of the DC-current reference, i.e., $i_{\rm dc} = i^\star_{\rm dc}$ in (2a).

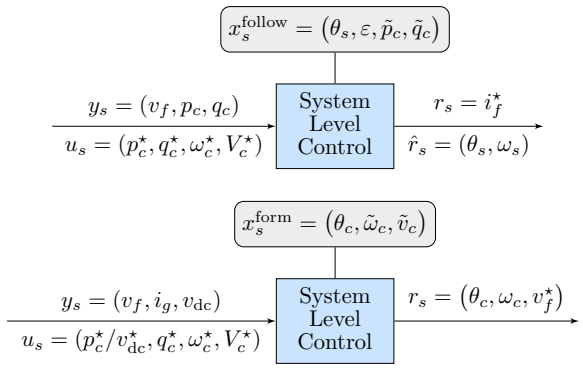

Fig. 3. Simplified MIMO structure of the system-level control: *grid-following* operation mode (top) and *grid-forming* operation mode (bottom).

for simplicity. Therefore, the remainder of this paper will focus only on droop control as a mean of system-level regulation.

Grid-Following Control: The two converter modes are fundamentally different. In the context of *grid-following* control, the measurements $y_s = (v_f, p_c, q_c) \in \mathbb{R}^4$ are commonly the output voltage and the active and reactive power. Moreover, (6) models a synchronization device - usually a PLL - that estimates the phase angle $\theta_s \in [-\pi, \pi)$ of the voltage v_f as well as the synchronous (grid) frequency $\omega_s \in \mathbb{R}_{>0}$ at the Point of Common Coupling (PCC), and provides them as reference $\hat{r}_s = (\theta_s, \omega_s)$ to the device-level control (see Fig. 3). Additionally, the so-called outer control loop is used to calculate the current reference $i_f^\star \in \mathbb{R}^2$ based on the mismatch between measured signals y_s and prescribed setpoints u_s. Hence, the system-level controller is described by $x_s^{\rm follow} = (\theta_s, \varepsilon, \tilde{p}_c, \tilde{q}_c) \in \mathbb{R}^4$, where $\tilde{p}_c \in \mathbb{R}$ and $\tilde{q}_c \in \mathbb{R}$ are the internal states corresponding to active and reactive power, respectively. Since the angle (θ_s) and frequency (ω_s) references are measured and passed through to device-level control (i.e., they are not regulated by an appropriate control law), we do not include them into the main output reference vector r.

The most common PLL implementation is a so-called type-2 SRF PLL [51], which achieves synchronization by diminishing the q-component $v_f^q \in \mathbb{R}$ of the voltage via PI control, thus aligning the d-axis of the Synchronously-rotating Reference Frame (SRF) with the output voltage vector v_f [7], [9], [10]:

$$\dot{\varepsilon} = v_f^q, \tag{7a}$$

$$\omega_s = \omega_0 + K_P^s v_f^q + K_I^s \varepsilon, \tag{7b}$$

$$\dot{\theta}_s = \omega_b \omega_s. \tag{7c}$$

Here, (K_P^s, K_I^s) are the proportional and integral control gains of the synchronization unit, $\omega_0 = 1\,\text{p.u.}$ is the nominal angular frequency, and $\varepsilon \in \mathbb{R}$ is the integrator state. Note that the *grid-following* converters require an established three-phase voltage at the connection terminal in order to obtain a reasonable frequency (i.e., angle) signal. Therefore, they do not posses standalone nor black start capabilities.

Having determined the synchronous angle and frequency (θ_s, ω_s), the outer control loop subsequently computes the current reference $i_f^\star \in \mathbb{R}^2$. By employing frequency and voltage droop control ($R_c^\omega \in \mathbb{R}_{\geq 0}$, $R_c^v \in \mathbb{R}_{\geq 0}$) in combination with integral controllers $K_{I,f}^d \in \mathbb{R}_{>0}$ and $K_{I,f}^q \in \mathbb{R}_{>0}$, the outer control loop, described by internal states variables $(\tilde{p}_c, \tilde{q}_c)$, regu-

0885-8950 (c) 2021 IEEE. Personal use is permitted, but republication/redistribution requires IEEE permission. See http://www.ieee.org/publications_standards/publications/rights/index.html for more information.
Authorized licensed use limited to: Cyprus University of Technology. Downloaded on March 18,2021 at 09:27:38 UTC from IEEE Xplore. Restrictions apply.

lates the power output (p_c, q_c) to its respective setpoint $(p_c^\star, q_c^\star)$, as follows:

$$\dot{\tilde{p}}_c = K_{I,f}^d \left(p_c^\star - p_c - R_c^\omega \left(\omega_s - \omega_c^\star\right)\right), \tag{8a}$$

$$\dot{\tilde{q}}_c = K_{I,f}^q \left(q_c^\star - q_c - R_c^v \left(\|v_f\| - V_c^\star\right)\right). \tag{8b}$$

Due to the $P-f$ and $Q-V$ droop characteristics, the active power reference is adjusted in response to a deviation of the measured frequency ω_s with respect to the frequency setpoint $\omega_c^\star$, whereas the reactive power reference is modified according to the mismatch between the magnitude of the output voltage $\|v_f\|$ and the converter voltage setpoint $V_c^\star$. Hence, the internal state vector of the system-level controller is $x_s^{\text{follow}} = (\theta_s, \omega_s, \tilde{p}_c, \tilde{q}_c) \in \mathbb{R}^4$, with $\tilde{p}_c$ and $\tilde{q}_c$ representing the power (i.e., dq-current) references. It should be pointed out that the controller (8) can take different forms, varying from a traditional frequency/AC-voltage droop control [14] and droop control with a low-pass filter [10] to DC-energy/reactive power droop control [52].

The computed power references are then transformed into the corresponding current reference signal $r_s = i_f^\star$, with two commonly used implementations for balanced systems: a constant current and a constant power mode. The first approach directly feeds the power references to the device-level control $i_f^\star = (\tilde{p}_c, \tilde{q}_c)$, while the second mode adjusts them based on output voltage measurement such that the converter's power output is kept constant:

$$i_f^{\star\, d} = \frac{v_f^d \tilde{p}_c + v_f^q \tilde{q}_c}{\|v_f\|}, \quad i_f^{\star\, q} = \frac{v_f^q \tilde{p}_c - v_f^d \tilde{q}_c}{\|v_f\|}. \tag{9}$$

Grid-Forming Control: Droop control is the prevalent control scheme for parallel *grid-forming* converters [53]–[55]. It achieves synchronization through measuring power imbalance and is inspired by the traditional primary frequency control of a synchronous machine. In particular, by appropriately adjusting the individual droop factors, it enables self-synchronization through the power grid and power sharing in proportion to the converter rating, while using only local measurements. Droop control is given by

$$\omega_c = \omega_c^\star + \underbrace{R_c^p \lambda_z(s) \left(p_c^\star - p_c\right)}_{\tilde{\omega}_c} \tag{10a}$$

$$v_c^d = V_c^\star + \underbrace{R_c^q \lambda_z(s) \left(q_c^\star - q_c\right)}_{\tilde{v}_c}, \tag{10b}$$

with $R_c^p \in \mathbb{R}_{>0}$ and $R_c^q \in \mathbb{R}_{\geq 0}$ being the droop gains, $\lambda_z \theta(s) = \frac{\omega_z}{\omega_z + s}$ representing the low-pass filter applied to the power measurements, $\omega_z \in \mathbb{R}_{>0}$ denoting its cut-off frequency, $\dot{\theta}_c = \omega_b \omega_c$ and $v_c^q = 0$. We emphasize that, unlike for the *grid-following* operation mode, in this case the angle θ_c, frequency $\tilde{\omega}_c \in \mathbb{R}$, and voltage $\tilde{v}_c \in \mathbb{R}$ are internal states of the control. In contrast, the active active and reactive power injections p_c and q_c are measured, i.e., $y_s = (p_c, q_c) \in \mathbb{R}^2$. Therefore, the control state vector can be defined as $x_s^{\text{form}} = (\theta_c, \tilde{\omega}_c, \tilde{v}_c)$, where

$$\dot{\tilde{\omega}}_c = -\omega_z \tilde{\omega}_c + R_c^p \omega_z (p_c^\star - p_c), \tag{11a}$$

$$\dot{\tilde{v}}_c = -\omega_z \tilde{v}_c + R_c^q \omega_z (q_c^\star - q_c). \tag{11b}$$

3) Device-Level Control: We start off by analyzing the device-level control of *grid-forming* converters, with a general structure presented in Fig. 4. This control layer provides both AC and DC-side reference signals for the VSC device. The AC-side controller operates in a synchronously-rotating dq-frame, with the reference angle θ_c and velocity ω_c provided by the system-level control (6). In particular, given a voltage reference $v_f^\star \in \mathbb{R}^2$ in dq-coordinates defined by (θ_c, ω_c), the device-level control is described by a cascade of voltage and current controllers (also called inner control loops) computing a switching voltage reference $v_{\text{sw}}^\star \in \mathbb{R}^2$ [5], [46]. More precisely, it encompasses a PI voltage controller

$$\dot{\xi} = v_f^\star - v_f, \tag{12a}$$

$$i_f^\star = K_P^v (v_f^\star - v_f) + K_I^v \xi + K_F^v i_g + j\omega_c c_f v_f, \tag{12b}$$

that provides an internal current reference $i_f^\star$ for a current PI controller

$$\dot{\gamma} = i_f^\star - i_f, \tag{13a}$$

$$v_{\text{sw}}^\star = K_P^i (i_f^\star - i_f) + K_I^i \gamma + K_F^i v_f + j\omega_c \ell_f i_f, \tag{13b}$$

where $(K_P^v, K_P^i) \in \mathbb{R}^2_{>0}$, $(K_I^v, K_I^i) \in \mathbb{R}^2_{\geq 0}$ and $(K_F^v, K_F^i) \in \mathbb{Z}^2_{\{0,1\}}$ are the respective proportional, integral, and feed-forward gains, $\xi \in \mathbb{R}^2$ and $\gamma \in \mathbb{R}^2$ represent the integrator states, and superscripts v and i denote the voltage and current controllers [9], [22], [56]. Note that the angular velocity ω_c of an SRF is reflected in the last terms of (12b) and (13b).

Finally, the DC voltage is controlled through the DC-current source and a PI controller, as follows:

$$\dot{\chi} = v_{\text{dc}}^\star - v_{\text{dc}}, \tag{14a}$$

$$i_{\text{dc}} = K_P^{\text{dc}} (v_{\text{dc}}^\star - v_{\text{dc}}) + K_I^{\text{dc}} \chi + K_F^{\text{dc}} i_{\text{dc}}^\star, \tag{14b}$$

with DC-voltage setpoint $u_d = v_{\text{dc}}^\star \in \mathbb{R}_{>0}$ being an external control input, $\chi \in \mathbb{R}$ the internal state variable, and proportional, integral, and feed-forward gains denoted by $K_P^{\text{dc}} \in \mathbb{R}_{>0}$, $K_I^{\text{dc}} \in \mathbb{R}_{\geq 0}$, and $K_F^{\text{dc}} \in \{0, 1\}$, respectively. The DC current reference $i_{\text{dc}}^\star \in \mathbb{R}_{>0}$ is determined by the operating point $(V_c^\star, p_c^\star, q_c^\star)$ and the converter losses, which indicates that for $v_{\text{dc}} = v_{\text{dc}}^\star$ the DC-side current will be $i_{\text{dc}} = i_{\text{dc}}^\star$.

Having computed the AC current and voltage $(i_f^\star, v_{\text{sw}}^\star)$ and DC current $(i_{\text{dc}}^\star)$ reference signals, the device-level control output $r_d = (\theta_r, \omega_r, v_{\text{sw}}^\star, i_{\text{dc}}^\star)$ is sent to the power converter, with $(\theta_r, \omega_r) = (\theta_c, \omega_c)$ being the angular reference adopted from the system-level control. The state vector of the controller is described by $x_d = (\xi, \gamma, \chi) \in \mathbb{R}^5$. In contrast, the system-level controller of a *grid-following* converter provides filter current reference. Therefore, the device-level control only comprises AC and DC current computation given by (13)-(14) (i.e., $x_d = (\gamma, \chi) \in \mathbb{R}^3$), thus bypassing the inner voltage controller. The output reference vector $r_d = (\theta_s, \omega_s, v_{\text{sw}}^\star, i_{\text{dc}}^\star)$ is provided to the power converter model, with $(\theta_r, \omega_r) = (\theta_s, \omega_s)$ being the measured angle and frequency references obtained by a synchronization unit within the system-level control.

4) Uniform Converter Model: In order to facilitate an ODE form of an arbitrary, generic low-inertia system, we propose a uniform converter model that comprises both *grid-forming* and *grid-following* mode of operation within a single control structure. More precisely, we modify the latter control design (both in terms of system- and device-level control) such that it fits the input-output characteristic of a *grid-forming* VSC while

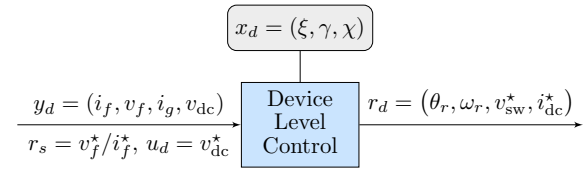

Fig. 4. Simplified MIMO structure of the device-level control.

0885-8950 (c) 2021 IEEE. Personal use is permitted, but republication/redistribution requires IEEE permission. See http://www.ieee.org/publications_standards/publications/rights/index.html for more information.
Authorized licensed use limited to: Cyprus University of Technology. Downloaded on March 18,2021 at 09:27:38 UTC from IEEE Xplore. Restrictions apply.

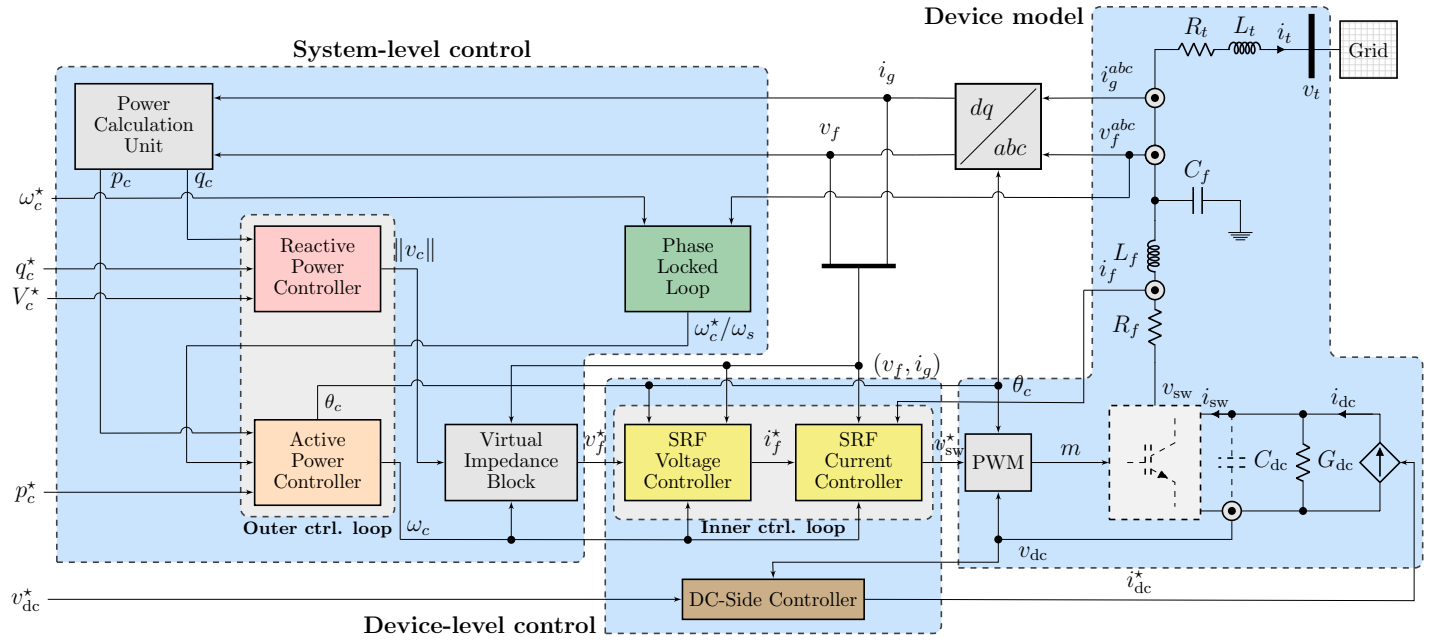

Fig. 5. General configuration of the implemented uniform VSC control structure.

still preserving its original dynamical properties. The general configuration of the implemented control scheme is illustrated[2] in Fig. 5, with three main segments (i.e., system-level control, device-level control and device model) corresponding to the block diagram in Fig. 1. However, the PLL has no function in the *grid-forming* operation, as it is bypassed and the frequency setpoint $\omega_c^\star$ is directly fed to the Active Power Controller (APC). Furthermore, the virtual impedance embeds an additional degree of freedom for active stabilization and disturbance rejection by providing a minor cross-coupling between d- and q-components via the resistive and inductive elements r_v and ℓ_v. This is achieved by computing a new voltage reference

$$v_f^\star = v_c - (r_v I_2 + j\omega_0 \ell_v) i_f, \tag{15}$$

and passing it through to the device-level control.

In terms of *grid-following* operation, the main distinction lies in the system-level control design, i.e., the droop implementation of the outer control loop. Instead of applying the controller (8) and drooping the frequency and voltage imbalance in order to determine the power (i.e., current) references, we employ a *grid-forming* control law given by (10). However, the frequency and voltage setpoint inputs $(\omega^\star, V^\star) := (\omega_c^\star, V_c^\star)$ are replaced by measurements $(\omega^\star, V^\star) := (\omega_s, \|v_f\|)$. Furthermore, we introduce the terms for low-pass filtered active and reactive power

$$\tilde{p}_c = \frac{\omega_z}{\omega_z + s} p_c, \quad \tilde{q}_c = \frac{\omega_z}{\omega_z + s} q_c, \tag{16}$$

and, by neglecting the low-pass filtering of constant setpoints $p_c^\star$ and $q_c^\star$, obtain

$$\omega_c = \omega^\star + R_c^p \left(p_c^\star - \tilde{p}_c\right), \quad v_c^d = V^\star + R_c^q \left(q_c^\star - \tilde{q}_c\right). \tag{17}$$

Although it does not meet the input-output criteria depicted in Fig 3, the presented *grid-following* control still achieves power reference tracking while simultaneously supporting the voltage and frequency at the PCC. In contrast to the controller (8), where the active power setpoint is adjusted according to the frequency mismatch, the droop control in (17) ensures that the power output meets its predefined setpoint by adjusting the reference frequency and voltage accordingly. Furthermore, such uniform structure implies that the same cascaded device-level control can be used for both converter modes. Therefore, the proposed uniform model can be described by (4)-(5) and (12)-(17) for the *grid-forming* mode and (4)-(5), (7) and (12)-(17) for the *grid-following* mode of operation, resulting in the 14^{th} and 16^{th}-order models, respectively. Clearly, the only difference between the two models is the presence of PLL dynamics (i.e., controller states ε and θ_s) in the latter one. The most relevant model and control tuning parameters are provided in Table I. Note that the MATLAB SIMULINK version of the model comprising several system-level controls is publicly available [57].

TABLE I
CONVERTER CONTROL PARAMETERS.

Parameter	Symbol	Value	Unit
Active power droop gain	R_c^p	2	%
Reactive power droop gain	R_c^q	0.1	%
LPF cut-off frequency	f_z	5	Hz
RLC filter resistance	r_f	0.03	p.u.
RLC filter inductance	ℓ_f	0.08	p.u.
RLC filter capacitance	c_f	0.074	p.u.
P-gain of SRF current control	K_P^i	0.74	-
I-gain of SRF current control	K_I^i	1.19	-
FF-gain of SRF current control	K_F^i	0	-
P-gain of SRF voltage control	K_P^v	0.52	-
I-gain of SRF voltage control	K_I^v	1.16	-
FF-gain of SRF voltage control	K_F^v	1	-
PLL proportional gain	K_P^s	0.4	-
PLL integral gain	K_I^s	4.69	-
Virtual impedance resistance	r_v	0.001	p.u.
Virtual impedance inductance	ℓ_v	0.2	p.u.

[2]Colored blocks in Fig. 5 indicate the presence of internal control dynamics.

0885-8950 (c) 2021 IEEE. Personal use is permitted, but republication/redistribution requires IEEE permission. See http://www.ieee.org/publications_standards/publications/rights/index.html for more information.
Authorized licensed use limited to: Cyprus University of Technology. Downloaded on March 18,2021 at 09:27:38 UTC from IEEE Xplore. Restrictions apply.

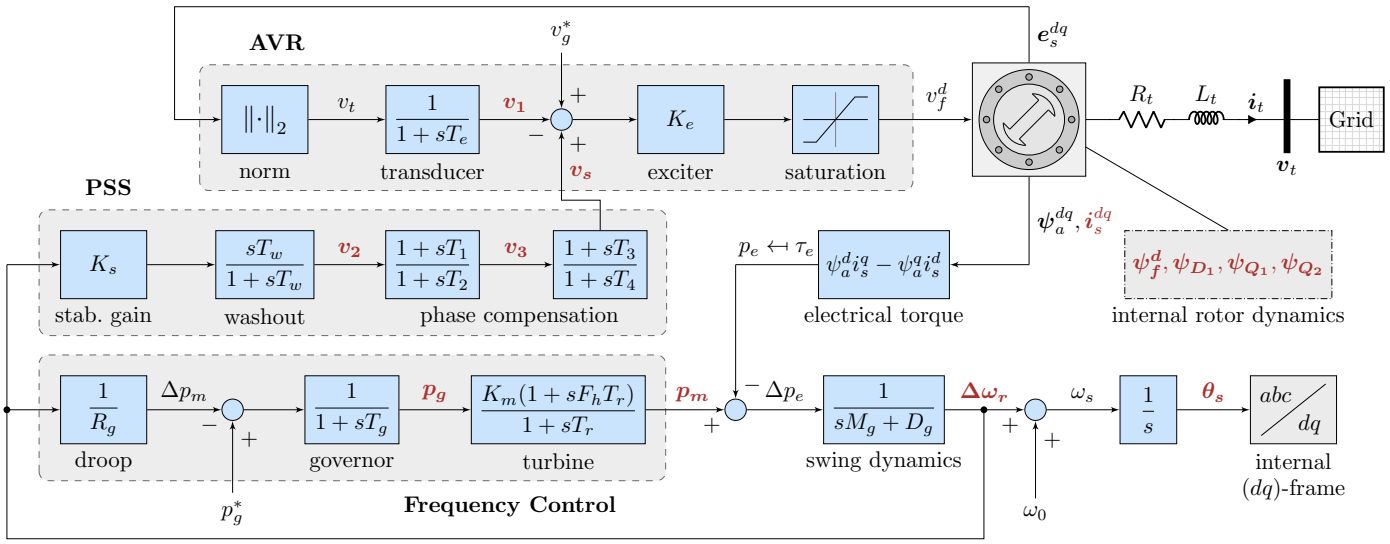

Fig. 6. Block diagram of a synchronous generator equipped with a prime mover, a governor and a voltage excitation system. The internal state variables are denoted by red color.

TABLE II
SYNCHRONOUS GENERATOR PARAMETERS.

Parameter	Symbol	Value	Unit
Droop control gain	R_g	2	%
Governor time constant	T_g	0.5	s
Reheat time constant	T_r	10	s
Mechanical power gain factor	K_m	0.85	-
Turbine power fraction factor	F_h	0.1	-
Normalized inertia constant	M_g	13	s
Normalized damping factor	D_g	1	p.u.
Transducer time constant	T_e	0.05	s
AVR exciter control gain	K_e	200	–
Saturation minimum output	$V_f^{\min}$	0	p.u.
Saturation maximum output	$V_f^{\max}$	4	p.u.
PSS stabilization gain	K_s	5	-
Washout time constant	T_w	2	s
1^{st} lead-lag derivative time constant	T_1	0.25	s
1^{st} lead-lag delay time constant	T_2	0.03	s
2^{nd} lead-lag derivative time constant	T_3	0.15	s
2^{nd} lead-lag delay time constant	T_4	0.015	s

B. Synchronous Generator Model

In this paper, we consider a traditional two-pole synchronous generator equipped with a prime mover and a governor. Additionally, a voltage excitation system comprised of an Automatic Voltage Regulator (AVR) and a PSS is incorporated into the model. A detailed block diagram of the SG model and its control scheme is illustrated in Fig. 6, where the generator is connected to the grid through a transformer modeled as a series impedance. The complete model is described in an SRF defined by generator's synchronous velocity and expressed in per-unit, with the main parameters provided in Table II.

1) Internal Machine Dynamics: The internal machine dynamics are characterized by the swing dynamics of the rotor as well as the transients in the rotor circuits, as transients in the stator windings decay rapidly and can thus be neglected. The swing dynamics are traditionally represented by the swing equation

$$M_g \Delta\dot{\omega}_r = \Delta p_e - D_g \Delta\omega_r, \tag{18}$$

with $M_g \in \mathbb{R}_{>0}$ and $D_g \in \mathbb{R}_{>0}$ being the normalized inertia and damping constants, $\Delta\omega_r \in \mathbb{R}$ denoting the deviation of rotor's angular velocity from the nominal value, and $\Delta p_e \in \mathbb{R}$ describing the mismatch between the mechanical power generated by the turbine and the electrical power at the SG's output.

On the other hand, rotor circuit dynamics originate in the armature reaction, i.e., in the effect of the stator field on the rotor currents, which can be described through flux linkage dynamics:

$$\dot{\psi}_f^d = \frac{\omega_0 r_f}{x_{a,u}^d} v_f^d - \frac{\omega_0 r_f}{x_f}\left(\psi_f^d - \psi_a^d\right), \tag{19a}$$

$$\dot{\psi}_{D_1} = -\frac{\omega_0 r_{D_1}}{x_{D_1}}\left(\psi_{D_1} - \psi_a^d\right), \tag{19b}$$

$$\dot{\psi}_{Q_1} = -\frac{\omega_0 r_{Q_1}}{x_{Q_1}}\left(\psi_{Q_1} - \psi_a^q\right), \tag{19c}$$

$$\dot{\psi}_{Q_2} = -\frac{\omega_0 r_{Q_2}}{x_{Q_2}}\left(\psi_{Q_2} - \psi_a^q\right). \tag{19d}$$

Here, subscripts f, D_1, Q_1 and Q_2 stand for the quantities of the field circuit, d-axis damping circuit and two q-axis damping circuits respectively, whereas $\psi \in \mathbb{R}^2$, $r \in \mathbb{R}_{>0}$ and $x \in \mathbb{R}_{>0}$ denote the respective flux linkage, resistance and reactance of a circuit. Moreover, $v_f \in \mathbb{R}^2$ is the exciter's output voltage with zero q-component (i.e., $\|v_f\| = v_f^d$), $\omega_0 \in \mathbb{R}_{>0}$ designates the synchronous angular velocity, and $x_{a,u}^d \in \mathbb{R}_{>0}$ stands for the unsaturated mutual reactance. Superscripts d and q are omitted from damping circuit quantities for simplicity, i.e., $\psi_{D_1} \in \mathbb{R}$, $\psi_{Q_1} \in \mathbb{R}$ and $\psi_{Q_2} \in \mathbb{R}$. The dq-components of the armature flux linkage $\psi_a \in \mathbb{R}^2$ are expressed as

$$\psi_a^d = \hat{x}_{a,s}^d \left(-i_s^d + \frac{\psi_f^d}{x_f} + \frac{\psi_{D_1}}{x_{D_1}}\right), \tag{20a}$$

$$\psi_a^q = \hat{x}_{a,s}^q \left(-i_s^q + \frac{\psi_{Q_1}}{x_{Q_1}} + \frac{\psi_{D_1}}{x_{Q_2}}\right), \tag{20b}$$

with the subtransient, saturated, mutual reactances $\hat{x}_{a,s}^d \in \mathbb{R}_{>0}$

0885-8950 (c) 2021 IEEE. Personal use is permitted, but republication/redistribution requires IEEE permission. See http://www.ieee.org/publications_standards/publications/rights/index.html for more information.
Authorized licensed use limited to: Cyprus University of Technology. Downloaded on March 18,2021 at 09:27:38 UTC from IEEE Xplore. Restrictions apply.

and $\hat{x}^q_{a,s} \in \mathbb{R}_{>0}$ defined by

$$\hat{x}^d_{a,s} = \left(\left(x^d_{a,s}\right)^{-1} + x_f^{-1} + x_{D_1}^{-1} \right)^{-1}, \tag{20c}$$

$$\hat{x}^q_{a,s} = \left(\left(x^q_{a,s}\right)^{-1} + x_{Q_1}^{-1} + x_{Q_2}^{-1} \right)^{-1}. \tag{20d}$$

Finally, the inclusion of stator's circuit balance completes the internal generator model:

$$e^d_s = -r_a i^d_s + x_l i^q_s - \psi^q_a, \tag{21a}$$

$$e^q_s = -r_a i^q_s + x_l i^d_s - \psi^d_a. \tag{21b}$$

In (21), stator voltage and current vectors are denoted by $e_s \in \mathbb{R}^2$ and $i_s \in \mathbb{R}^2$, while $r_a \in \mathbb{R}_{>0}$ and $x_l \in \mathbb{R}_{>0}$ represent the armature resistance and leakage reactance respectively. Expressions (18)-(21) yield a 6^{th}-order dynamical model described by the state vector $x_g^{\text{int}} := \left(\theta_s, \omega_s, \psi^d_f, \psi_{D_1}, \psi_{Q_1}, \psi_{D_2}\right) \in \mathbb{R}^6$, where $\dot{\theta}_s = \omega_b \omega_s$. For more details regarding the generator modeling and internal parameter computation we refer the reader to [2].

2) Control Design and Electrical Interface: The proposed control scheme comprises two independent loops for frequency and voltage regulation [58]. The former one consists of droop control and governor and turbine dynamics (see Fig. 6), described respectively by state variables $p_g \in \mathbb{R}$ and $p_m \in \mathbb{R}$ (i.e., a state vector $x_g^{\text{freq}} = (p_g, p_m) \in \mathbb{R}^2$). On the other hand, voltage control includes an AVR with a transducer and a saturated exciter, and a PSS combining a washout filter and a lead-lag phase compensation, with vectors $x_g^{\text{AVR}} := v_1 \in \mathbb{R}$ and $x_g^{\text{PSS}} := (v_2, v_3, v_s) \in \mathbb{R}^3$ describing the underlying controller states respectively. For brevity, we will omit a detailed derivation of the control dynamics pertaining to frequency control, AVR and PSS, as it can be easily deduced from the control block diagram in Fig. 6. Note that all state variables are denoted by red color in Fig. 6.

As mentioned previously, a synchronous generator is interfaced to the grid through a transformer modeled as a series impedance $r_t \in \mathbb{R}_{>0}$ and $\ell_t \in \mathbb{R}_{>0}$. The dynamics of the current $i_t \in \mathbb{R}^2$ flowing through a transformer can be expressed in an SRF defined by (θ_s, ω_s) as

$$\dot{i}_t = \frac{\omega_b}{\ell_t}(e_s - v_t) - \left(\frac{r_t}{\ell_t}\omega_b + j\omega_b\omega_s \right) i_s, \tag{22}$$

where $v_t \in \mathbb{R}^2$ denotes the terminal voltage and terminal current corresponds to stator current (i.e., $i_s := i_t$). Finally, by combining (18)-(22) with the dynamics of frequency and voltage control loops, we obtain a 14^{th}-order SG model described by the state vector $x_g = \left(x_g^{\text{int}}, x_g^{\text{freq}}, x_g^{\text{AVR}}, x_g^{\text{PSS}}, i_t\right) \in \mathbb{R}^{14}$.

C. Network and System Modeling

1) Transmission Network Dynamics: Modeling of the transmission network is described for a generic system depicted in Fig. 7, composed of generators supplying local RL loads and the interconnecting transmission lines modeled as π-sections; long transmission lines with lengths above $250\,\text{km}$ are represented by distributed line parameters. In order to establish a consistent mathematical formulation, all variables have to be defined within a single SRF, including the reference frame of the network. Neglecting grid dynamics has been a general assumption for SG-dominated power systems, based on the premise of grid and and generator's armature dynamics being much faster than those of the excitation and governor systems [59], [60]. Alternatively, studies often oversimplify the problem and assume that the grid's

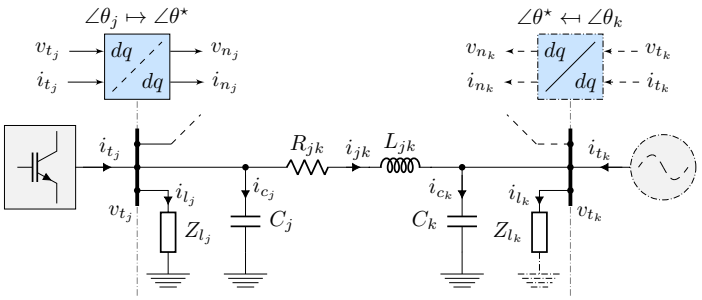

Fig. 7. Generic network model with line dynamics and respective dq-frame alignment.

SRF rotates at constant nominal angular velocity, as pointed out in [19].

Let us introduce a transformation $f_n : \mathbb{Z}_{>0} \mapsto \mathbb{Z}_{>0}$ that maps the set of generator indices $g \in \mathcal{G} \subset \mathbb{Z}_{>0}$ to the subset of nodal indices of the network with generator connection $j \in \mathcal{N}_g \subset \mathcal{N}$, with $\mathcal{N} \subset \mathbb{Z}_{>0}$ being the index set of network nodes. Hence, the terminal currents[3] $i_{t_g} \in \mathbb{R}^2$ and voltages $v_{t_g} \in \mathbb{R}^2$ of each generator unit $g \in \mathcal{G}$ are mapped to vectors $i_{t_j} \in \mathbb{R}^2$ and $v_{t_j} \in \mathbb{R}^2$ corresponding to the terminal currents and voltages of the network nodes $j \in \mathcal{N}_g$, where $j = f_n(g)$. The nodal vectors are subsequently aligned to the SRF of an arbitrary synchronous generator or a *grid-forming* converter $r \in \mathcal{G}$, rotating at angular speed $\omega^\star := \omega_{s_r}$, i.e., $\omega^\star := \omega_{c_r}$, as follows:

$$x_{n_j} = \mathcal{R}\left(\theta^\star - \theta_j\right) x_{t_j}, \, \forall j \in \mathcal{N}. \tag{23}$$

Here, $x_{n_j} \in \{i_{n_j}, v_{n_j}\}$ denotes the "nodal" metrics described in the nominal reference frame, the uniform SRF angle is computed as $\dot{\theta}^\star = \omega_b \omega^\star$, and $\theta_j \in [-\pi, \pi)$ corresponds to the internal SRF angle of the respective unit, i.e., $\theta_j := \theta_{s_j}$ for the synchronous and $\theta_j := \theta_{c_j}$ for the converter-based generator. According to [59], [61], such approach provides a good trade-off between the computational complexity and model accuracy.

The nodal voltage and current dynamics can now be expressed $\forall j \in \mathcal{N}$ as

$$\dot{v}_{n_j} = \frac{\omega_b}{c_{l_j}} i_{c_j} - j\omega_b \omega^\star v_{n_j}, \tag{24a}$$

$$\dot{i}_{l_j} = \frac{\omega_b}{\ell_{l_j}} v_{n_j} - \left(\frac{r_{l_j}}{\ell_{l_j}}\omega_b + j\omega_b\omega^\star \right) i_{l_j}, \tag{24b}$$

thus capturing the load and shunt phenomena at each node, with $r_{l_j} \in \mathbb{R}_{>0}$ and $\ell_{l_j} \in \mathbb{R}_{>0}$ being the load's resistance and inductance, and $c_j \in \mathbb{R}_{>0}$ reflecting the aggregate shunt capacitance. Finally, the line dynamics are represented using a conventional RL circuit formulation

$$\dot{i}_{jk} = \tfrac{\omega_b}{\ell_{jk}}(v_{n_j} - v_{n_k}) - \left(\tfrac{r_{jk}}{\ell_{jk}}\omega_b + j\omega_b\omega^\star \right) i_{jk}, \, \forall j \in \mathcal{N}, k \in \mathcal{K}_j, \tag{25}$$

with $i_{jk} \in \mathbb{R}^2$ being the current and $(r_{jk}, \ell_{jk}) \in \mathbb{R}^2_{>0}$ the respective parameters of a transmission line connecting nodes $j \in \mathcal{N}$ and $k \in \mathcal{K}_j$, and $\mathcal{K}_j \subset \mathcal{N}$ denoting the subset of nodes adjacent to node j. Combining (23)-(25) with the algebraic expressions for current balance at each node $j \in \mathcal{N}$ in the system concludes the network model.

[3]Note that the terminal currents correspond to stator currents i_s of SGs (see Fig. 6) or to grid injection currents i_g of VSCs (see Fig. 5).

0885-8950 (c) 2021 IEEE. Personal use is permitted, but republication/redistribution requires IEEE permission. See http://www.ieee.org/publications_standards/publications/rights/index.html for more information.
Authorized licensed use limited to: Cyprus University of Technology. Downloaded on March 18,2021 at 09:27:38 UTC from IEEE Xplore. Restrictions apply.

This article has been accepted for publication in a future issue of this journal, but has not been fully edited. Content may change prior to final publication. Citation information: DOI 10.1109/TPWRS.2021.3061434, IEEE Transactions on Power Systems

2) Complete Model Formulation: Having defined models of different generation units and the network, we can complete the general ODE formulation of the system. Let us consider a large-scale, low-inertia system with nodal and generation index sets $\mathcal{N}$ and $\mathcal{G}$ defined previously. Furthermore, let $\mathcal{S} \subset \mathbb{Z}_{>0}$ and $\mathcal{C} \subset \mathbb{Z}_{>0}$ ($\mathcal{S} \cup \mathcal{C} = \mathcal{G}$) be the index sets of synchronous and converter-interfaced generators, with the second set differentiating between the subsets $\mathcal{C}_{\mathrm{F}} \subset \mathcal{C}$ and $\mathcal{C}_{\mathrm{f}} \subset \mathcal{C}$ of *grid-forming* and *grid-following* units, respectively. Furthermore, let $\mathcal{B} \subset \mathbb{Z}_{>0}$ denote the index set of network branches, where elements of the branch current vector $i_b \in \mathbb{R}^{|\mathcal{B}|}$ are mapped to the currents i_{jk} in (25) using the transformation $f_i : \mathbb{Z}^2_{>0} \mapsto \mathbb{Z}_{>0}$ such that $\forall j \in \mathcal{N}, \forall k \in \mathcal{K}_j, \exists m \in \mathcal{B} \mid m = f_i(j,k) \wedge i_{b_m} \coloneqq i_{jk}$.

The dynamical model of such system can be expressed by

$$\dot{x} = f(x,u), \tag{26a}$$

where

$$x = \left(x^{\mathrm{F}}_{c_1}, \ldots, x^{\mathrm{F}}_{c_{|\mathcal{C}_{\mathrm{F}}|}}, x^{\mathrm{f}}_{c_1}, \ldots, x^{\mathrm{f}}_{c_{|\mathcal{C}_{\mathrm{f}}|}}, x_{g_1}, \ldots, x_{g_{|\mathcal{S}|}}, x_n\right), \tag{26b}$$

$$u = \left(u^{\mathrm{F}}_{c_1}, \ldots, u^{\mathrm{F}}_{c_{|\mathcal{C}_{\mathrm{F}}|}}, u^{\mathrm{f}}_{c_1}, \ldots, u^{\mathrm{f}}_{c_{|\mathcal{C}_{\mathrm{f}}|}}, u_{g_{|\mathcal{S}|}}\right). \tag{26c}$$

The state and control input vectors of *grid-forming* and *grid-following* converters (denoted by superscripts F and f respectively) in (26b)-(26c) are defined $\forall p \in \mathcal{C}_{\mathrm{F}}$ and $\forall q \in \mathcal{C}_{\mathrm{f}}$ as

$$x^{\mathrm{F}}_{c_p} = (i_f, v_f, i_g, \xi, \gamma, \chi, \tilde{p}_c, \tilde{q}_c, \theta_c) \in \mathbb{R}^{14}, \tag{26d}$$

$$x^{\mathrm{f}}_{c_q} = (i_f, v_f, i_g, \xi, \gamma, \chi, \varepsilon, \theta_s, \tilde{p}_c, \tilde{q}_c, \theta_c) \in \mathbb{R}^{16}, \tag{26e}$$

$$u^{\mathrm{F}}_{c_p} = (p^\star_c, q^\star_c, V^\star_c, \omega^\star_c, v^\star_{\mathrm{dc}}) \in \mathbb{R}^5, \tag{26f}$$

$$u^{\mathrm{f}}_{c_q} = (p^\star_c, q^\star_c, v^\star_{\mathrm{dc}}) \in \mathbb{R}^3. \tag{26g}$$

Moreover, the SGs in (26b)-(26c) are described $\forall r \in \mathcal{S}$ by

$$x_{g_r} = \left(\theta_s, \omega_s, \psi^d_f, \psi_{D_1}, \psi_{Q_1}, \psi_{D_2}, i_s, v_1, v_2, v_3, v_s, p_g, p_m\right) \in \mathbb{R}^{14}, \tag{26h}$$

$$u_{g_r} = \left(p^\star_g, v^\star_g\right) \in \mathbb{R}^2, \tag{26i}$$

and the state vector of network dynamics is expressed in the form

$$x_n = \left(v_{n_1}, \ldots, v_{n_{|\mathcal{N}|}}, i_{l_1}, \ldots, i_{l_{|\mathcal{N}|}}, i_{b_1}, \ldots, i_{b_{|\mathcal{B}|}}\right) \in \mathbb{R}^{4|\mathcal{N}|+2|\mathcal{B}|}. \tag{26j}$$

The final model order is therefore $N = 14|\mathcal{C}_{\mathrm{F}}| + 16|\mathcal{C}_{\mathrm{f}}| + 14|\mathcal{S}| + 4|\mathcal{N}| + 2|\mathcal{B}|$, whereas the control input vector comprises $M = 5|\mathcal{C}_{\mathrm{F}}| + 3|\mathcal{C}_{\mathrm{f}}| + 2|\mathcal{S}|$ setpoints.

The nonlinear ODE model (26) can also be represented in a linear form

$$\Delta\dot{x} = A\Delta x + B\Delta u \tag{27}$$

by linearizing (26a) around the steady-state point (x_0, u_0), with $A \in \mathbb{R}^{N\times N}$ and $B \in \mathbb{R}^{N\times M}$ being the state-space matrices, and Δ denoting small deviations around the equilibrium (x_0, u_0). Nevertheless, while providing accurate dynamical representation of the system, such linear model also leads to a minor steady-state error compared to its nonlinear counterpart. The mismatch can be seen in Fig. 8, showcasing a time-domain response of a two-generator system after a step increase in load demand. The steady-state error arises due to the linearization of the alignment, i.e., the approximation of trigonometric terms within the rotation matrix $\mathcal{R}(\cdot)$ in (23). This also explains why power, and hence the frequency, experience the highest mismatch, as they cumulatively absorb the errors pertaining to alignment of each individual voltage and current vector. Note that for a global SRF rotating at constant angular velocity $\omega^\star$, the formulation (27) is not feasible, i.e., the obtained linear model is unstable. This is again justified by the linearization of (23), which cannot accurately capture the alignment.

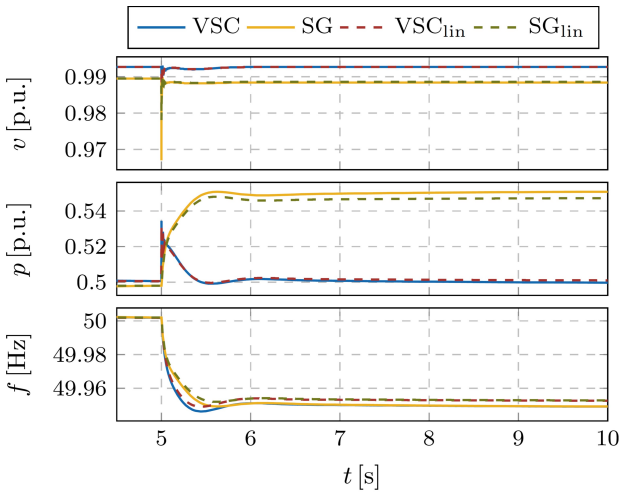

Fig. 8. Time-domain performance of nonlinear and linear model representation of a two-generator system after a load step change.

III. Timescales in Low-Inertia Systems

The overall complexity of dynamics pertaining to low-inertia systems is well described through characteristic timescales illustrated in Fig. 9. Conventional power systems based on synchronous generators have a distinct difference in time constants for frequency and voltage regulation, with turbines ($T_r \approx 10\,\mathrm{s}$) and governors ($T_g \approx 1\,\mathrm{s}$) operating on much longer timescales than the exciter ($T_e \approx 50\,\mathrm{ms}$) [58]. Moreover, swing and flux dynamics reflect the time constants of the swing equation and synchronous machine flux linkages, respectively. Considering that the time constants of the line dynamics vary in the $T_\ell \in [1-30]\,\mathrm{ms}$ range, depending on the network type, it is clear that the conventional control schemes would ensure system stability. However, with the inclusion of fast-acting converter-based generation, the system dynamics become more complex and convoluted and may lead to unexpected couplings [1]. For instance, the traditional assumption of neglecting fast line dynamics is not valid anymore, since the underlying dynamics are of the same order of magnitude as the ones of converter voltage control. On the other hand, the time constants of the PI controllers and low-pass filters associated with the inner and outer inverter control loops are one or two orders of magnitude smaller than the ones of the synchronous machines, potentially resulting in adverse control interference and instability, especially with high shares of renewables. Moreover, the time delays associated with Wide Area Monitoring Systems (WAMS) would make any type of emergency regulation without the use of high-speed fibre optics obsolete [62].

It should be noted that by voltage and frequency dynamics in Fig. 9 we refer to the controllers associated with voltage and frequency regulation, respectively. While somewhat related, these notions are not in direct correlation with the traditional voltage and frequency stability terms [63], especially considering the complex dynamics of low-inertia systems and a timescale separation between the controls of different unit types regulating the same system metric (voltage magnitude or frequency).

0885-8950 (c) 2021 IEEE. Personal use is permitted, but republication/redistribution requires IEEE permission. See http://www.ieee.org/publications_standards/publications/rights/index.html for more information.
Authorized licensed use limited to: Cyprus University of Technology. Downloaded on March 18,2021 at 09:27:38 UTC from IEEE Xplore. Restrictions apply.

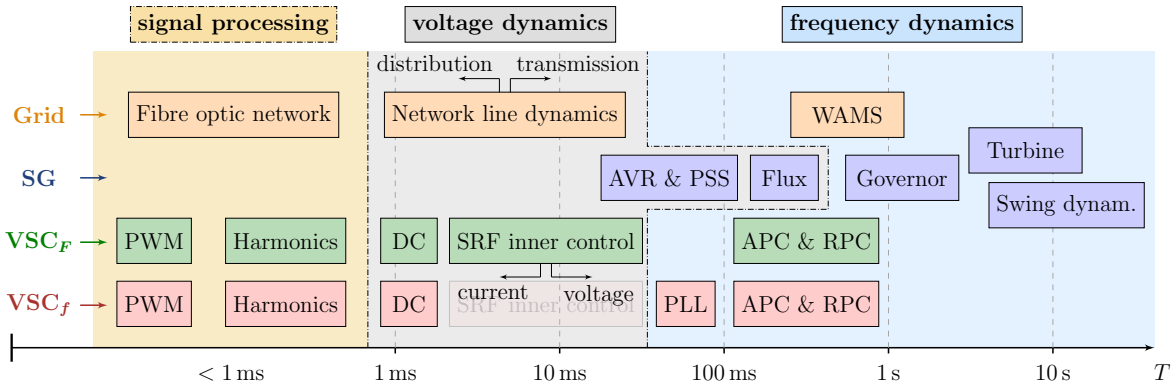

Fig. 9. Characteristic timescales of different physical and control dynamics in a low-inertia system.

We also note that the impact of network line dynamics becomes more profound in *inertialess* systems. Its effect on frequency stability can be illustrated by analyzing a uniform frequency control loop of an individual *grid-forming* inverter connected to $k \in \mathcal{K}_j$ adjacent inverter units as follows:

$$\tau_z \ddot{\theta}_{c_j} + \left(1 - \omega_b R_c^p B_j'\right) \dot{\theta}_{c_j} + \omega_b R_c^p B_j \theta_{c_j} + C_j = 0, \qquad (28)$$

with (ω_c, θ_c) denoting the converter frequency and phase angle, R_c^p being the active power droop, ω_b representing the base frequency, $C_j = \omega_b \omega_{c_j}^\star + \omega_b R_c^p p_{c_j}^\star$, and

$$B_j = \sum_{k \in \mathcal{K}_j} \frac{\omega_0 \ell_{jk}}{\omega_b \left(r_{jk}^2 + \omega_0^2 \ell_{jk}^2\right)^2}, \quad B_j' = \sum_{k \in \mathcal{K}_j} \frac{2 r_{jk} \ell_{jk}^2}{\omega_b \left(r_{jk}^2 + \omega_0^2 \ell_{jk}^2\right)^2}.$$

Here, ω_0 is the nominal per-unit frequency and (r_{jk}, ℓ_{jk}) denote the resistance and inductance of the transmission line between nodes j and k. The analytical derivation is omitted for brevity.

We also note that the impact of network line dynamics becomes more profound in *inertialess* systems. Its effect on frequency stability can be illustrated by analyzing a general frequency control loop of an individual *grid-forming* inverter $j \in \mathcal{N}_g$ connected to $|\mathcal{K}_j|$ VSC units $k \in \mathcal{K}_j$ adjacent to inverter j, as follows:

$$\tau_z \ddot{\theta}_{c_j} + \left(1 - \omega_b R_c^p B_j'\right) \dot{\theta}_{c_j} + \omega_b R_c^p B_j \theta_{c_j} + C_j = 0, \qquad (29)$$

with $C_j = \omega_b \omega_{c_j}^\star + \omega_b R_c^p p_{c_j}^\star$ and

$$B_j = \sum\nolimits_{k \in \mathcal{K}_j} \frac{\omega_0 \ell_{jk}}{\omega_b \left(r_{jk}^2 + \omega_0^2 \ell_{jk}^2\right)^2}, \quad B_j' = \sum\nolimits_{k \in \mathcal{K}_j} \frac{2 r_{jk} \ell_{jk}^2}{\omega_b \left(r_{jk}^2 + \omega_0^2 \ell_{jk}^2\right)^2}.$$

The derivation of underlying expressions is provided in Appendix B.

In order to preserve system synchronization, the natural negative feedback terms for θ_{c_j} and $\dot{\theta}_{c_j}$ must be positive, indicating an upper limit on the active power droop gain $R_c^p < (\omega_b B_j')^{-1}$. Such threshold is even more restrictive for distribution networks, due to shorter node distances and a lower ℓ_{jk}/r_{jk} line impedance ratio. Furthermore, the impact of the power network also pertains to inverter synchronization through θ_{cj} term, since very high feedback control gains $\kappa_j = \omega_b R_c^p B_j$ might lead to inverter frequency oscillations exciting the oscillatory modes of the transmission lines. In other words, the inverters achieve synchronization by inferring information about the phase angle differences through local measurements of currents and voltages. Therefore, the time constant of transmission lines can be interpreted as a propagation delay of the information on the phase angles, and the controllers cannot act faster than the time needed to observe information through the network. Hence, larger time constants require a lower feedback gain, which implies that reducing transmission line impedance ratio or increasing network connectivity can make a low-inertia system unstable. Similar remarks have been pointed out for microgrids comprising solely inverters based on droop [64] and dispatchable virtual oscillator control [65]. While we only focus on frequency dynamics in this example, it should be noted that the voltage dynamics could also be assessed using the proposed approach, as indicated in [64]–[66].

IV. Stability Properties of a Small System

A. Unit Interactions in a 2-bus Test System

For the first case study, we consider a simple 2-bus system with two generators connected over a transmission line and an RL load supplied at one node. The goal is to incorporate different units into the system and investigate their dynamic interactions and the respective stability margins. In order to confine the observed phenomena solely to the generators under study, the transmission line dynamics are neglected at this point, i.e., line connections are represented only by algebraic equations.

We investigate three different scenarios based on the generator type configuration: (i) a synchronous generator and a *grid-following* VSC; (ii) a synchronous generator and a *grid-forming* VSC; and (iii) a *grid-forming* and a *grid-following* VSC. Furthermore, we introduce a penetration ratio η, which describes the installed penetration level of inverter-based units. In the first two cases this corresponds to $\eta = p_c/(p_g + p_c)$, whereas in the last scenario this factor denotes the penetration of the *grid-following* generation, i.e., $\eta = p_{c_f}/(p_{c_F} + p_{c_f})$, with subscripts F and f representing the *grid-forming* and *grid-following* converters respectively. Note that all generators operate at $50\,\%$ of the installed capacity, i.e., $p^\star = 0.5\,\text{p.u.}$

The small-signal stability margins of different system configurations are illustrated in Fig. 10, where the stability is assessed through real-part movement of the most critical eigenvalue $\hat{\lambda}$. Understandably, the system comprising both synchronous generators and *grid-forming* inverters can withstand higher levels of PE-based devices ($\approx 79\%$), as the voltage phasors at both nodes are fully established and controlled by the local generators. Additionally, the synchronization and power sharing properties are inherently provided by both units. On the other hand, the penetration of *grid-following* generation adversely affects the system balance, and significantly reduces the maximum admissible ratio to $\eta_{\text{max}} \approx 60\,\%$ and $\eta_{\text{max}} \approx 59\,\%$ for Scenarios I and III, respectively. Scenario III also has a steeper progression of $\hat{\lambda}$,

0885-8950 (c) 2021 IEEE. Personal use is permitted, but republication/redistribution requires IEEE permission. See http://www.ieee.org/publications_standards/publications/rights/index.html for more information.
Authorized licensed use limited to: Cyprus University of Technology. Downloaded on March 18,2021 at 09:27:38 UTC from IEEE Xplore. Restrictions apply.

This article has been accepted for publication in a future issue of this journal, but has not been fully edited. Content may change prior to final publication. Citation information: DOI 10.1109/TPWRS.2021.3061434, IEEE Transactions on Power Systems

indicating that it is difficult to achieve a noticeable improvement of the critical penetration ratio.

As a second step, we thoroughly explore the fundamental components contributing to the aforementioned instability. This is achieved by determining the critical modes of the system, employing participation factor and parameter sensitivity analyses, and determining the states (i.e., the controllers) that predominantly contribute to such modes. Each of the proposed scenarios comprises a unique ODE system with specific dynamics. Therefore, all three system configurations are individually investigated and discussed in detail below:

1) Scenario I: It is observed that the inverter penetration above $60\,\%$ leads to system collapse. Interestingly, the instability initially originates in the voltage dynamics due to incompatibility of the VSC inner control loop and the generator's PSS, as illustrated in Fig. 11. Subsequently, the vulnerability spreads across the whole excitation system, including the AVR. At this point the system is heavily unstable. This phenomena comes from the time constants of the inner loops being drastically smaller than the ones of the exciter. More specifically, once the system becomes predominantly PE-based the "non-forming" aspect of the inverter's voltage phasor counteracts and diminishes the firm voltage at the SG terminal, thus weakening the system. For even higher VSC penetration levels ($> 75\,\%$) the network faces frequency stability issues, as the PLL, and subsequently the active power controller, cannot provide adequate synchronization of the *grid-following* units due to an insufficiently stiff global frequency signal.

By studying the movement of the critical eigenvalue spectrum in Fig. 11 we notice that the real part $\Re(\hat{\lambda})$ significantly increases for inverter shares above $68\,\%$. Considering that PSS and inner SRF controllers largely participate in critical modes for $\eta \in [60, 68]\ \%$, one can assume that tuning the respective control gains could restore system stability within this range. While the increase in PSS stabilization gain proves to be relatively beneficial for the system, the adjustment of inner loop PI controllers has no impact on the eigenvalue spectrum, as shown in Fig. 12. This is an expected outcome due to a large timescale separation between the two feedback loops, which in turn hinders the synchronous generation from providing a stiff voltage at the terminal. Furthermore, inner converter control loops are often predefined by the manufacturer and optimally designed for providing fast and accurate voltage and power reference tracking, implying that any parameter changes would distort its original purpose and effectiveness.

Beside the SG voltage regulators, the dynamics of the swing equation also prove to be relevant to a certain extent for the

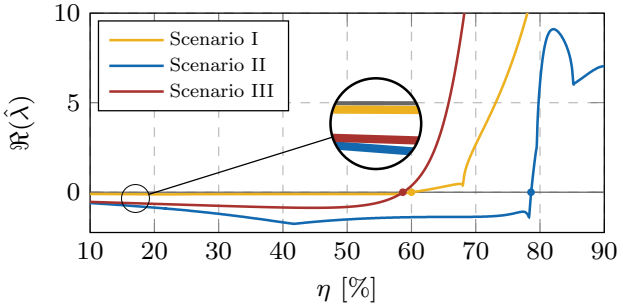

Fig. 10. Impact of inverter penetration on system stability for different unit configuration.

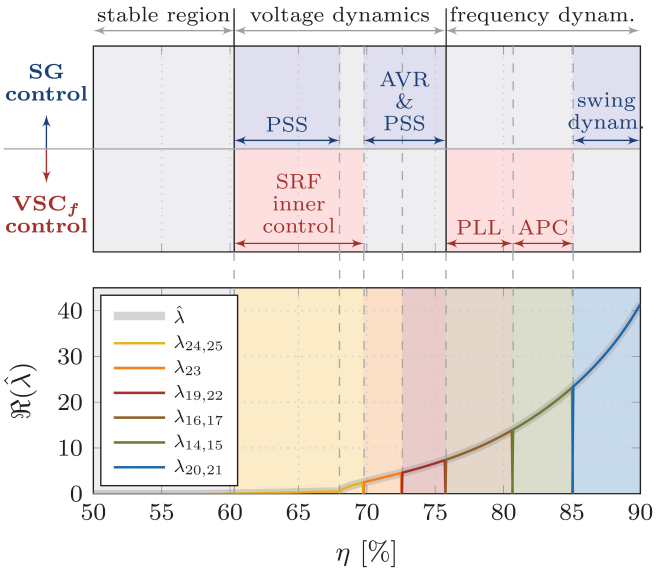

Fig. 11. Impact of different controllers on system stability under high *grid-following* inverter penetration in Scenario I.

overall stability. However, in contrast to the popular belief that low inertia levels lead to vulnerability, it is in fact the insufficient damping that propagates the problem. Similar to the PSS stabilization gain, the higher damping constant facilitates the integration of converters (see Fig. 12), whereas the inertia constant has no impact on the overall penetration; an observation that was also made in [40]. Nonetheless, damping is related to physical properties of synchronous generators, while droop gains, essentially corresponding to damping, are prescribed within narrow ranges by the grid codes. This suggests that the most viable and practical solution would be to improve the PSS design, i.e., increase its responsiveness, in order to accommodate a high penetration of *grid-following* inverter-based generation.

2) Scenario II: The issues pertaining to timescale separation between different voltage controllers already highlighted in the previous scenario remain also in this scenario. It can be noticed that the "forming" inverter property bolsters the voltage vector at the respective bus and drastically improves the stability margin of the system. Nonetheless, for $\eta > 78\,\%$ the AVR and PSS controllers cannot achieve adequate voltage stabilization, as the eigenvalues depicted in Fig. 13 are located deeply into the right-hand side of the root loci spectrum. Hence, the maximum feasible penetration of VSCs can hardly be improved. Another important observation is that the frequency dynamics are not contributing to instability anymore, since both units independently establish an adequate frequency signal and subsequently synchronize.

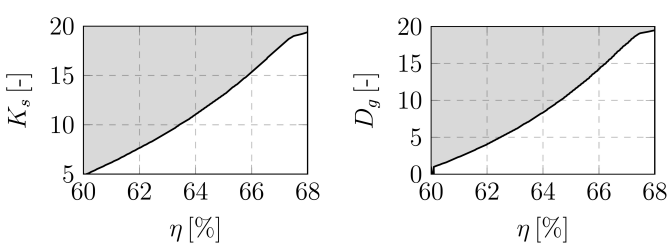

Fig. 12. Stability maps in $K_s - \eta$ and $D_g - \eta$ planes indicating the effect of PSS stabilization gain and SG damping on admissible penetration of *grid-following* inverter units in Scenario I.

0885-8950 (c) 2021 IEEE. Personal use is permitted, but republication/redistribution requires IEEE permission. See http://www.ieee.org/publications_standards/publications/rights/index.html for more information.
Authorized licensed use limited to: Cyprus University of Technology. Downloaded on March 18,2021 at 09:27:38 UTC from IEEE Xplore. Restrictions apply.

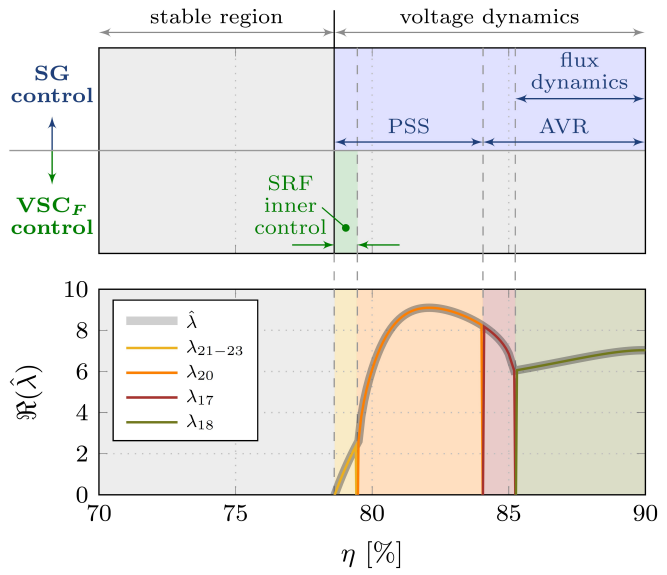

Fig. 13. Impact of different controllers on system stability under high *grid-forming* inverter penetration in Scenario II.

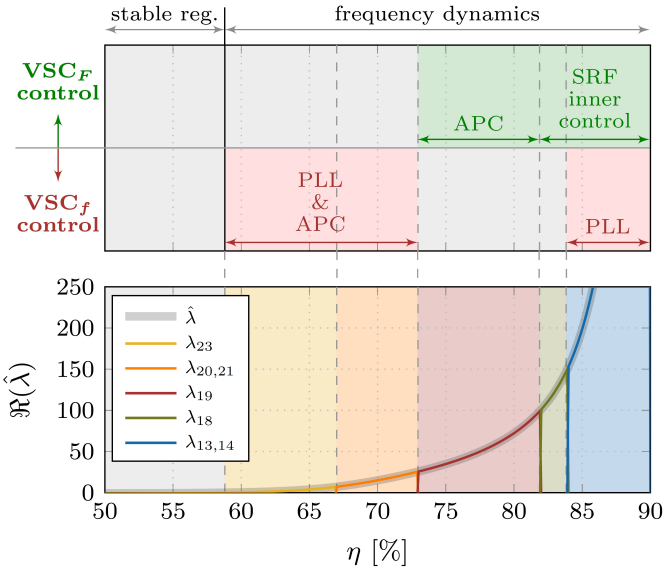

Fig. 14. Impact of different controllers on system stability under high *grid-following* inverter penetration in Scenario III.

3) Scenario III: We tackle the 100 % PE-based scenario by increasing the share of *grid-following* units (i.e., by increasing factor η), with the results presented in Fig. 14. The main distinction of this scenario is the elimination of voltage control issues in the presence of SGs and inverters, as both VSCs regulate voltage on the same timescale. In spite of improving the voltage dynamics in the system, the synchronization problems are aggravated due to an exclusion of a synchronous generator. In other words, the dedicated "forming" capability of a *grid-forming* converter is inferior to the one of a traditional generator. As a result, for penetration levels above $\approx 59\,\%$ the PLL units of *grid-following* inverters cannot accurately estimate the frequency signal, leading to failure in the active power control and preventing system-level synchronization. Similar properties are also reflected when analyzing η as a function of the proportional PLL gain, with a more responsive PLL potentially facilitating a higher penetration factor (see Fig. 15). However, this approach does not solve the fundamental problem at hand, and provides only a marginal improvement of a few percent. It should be noted that the integral gain of the respective PI controller does not affect the system stability margin, indicating that the original PLL time constant could be maintained in the process.

B. Inclusion of Transmission Line Dynamics

We broaden the scope of our analysis by including the transmission line dynamics. The same three scenarios are re-evaluated and compared against the previous case study, with the respective results illustrated in Fig. 16. A noticeable difference in the stability margin of a 100 % inverter-based system can be observed, where the inclusion of line dynamics significantly increases the maximum penetration ratio η. This can be explained by the inductive and capacitive components of the lines acting as energy buffers and augmenting the synchronization between the two units. More precisely, the frequency issues associated with a large proportion of PLL-based generation are alleviated through interactions with the LC segments of the transmission lines, which slows down the frequency dynamics and enables the *grid-following* VSCs to more accurately detect the weak frequency signal. Similar conclusions have been drawn for autonomous microgrids [67] and networks comprised of a specific class of *grid-forming* inverters [65], as well as in [3] using a mechanical analogue of swings in a multi-machine system.

On the other hand, the scenarios experiencing instability related to voltage dynamics are for the most part unaffected by the transmission line dynamics. The voltage control interaction between the synchronous and PE-based generation is somewhat mitigated, due to the time constants of the line dynamics and the SRF inner control loops being of the same order of magnitude.

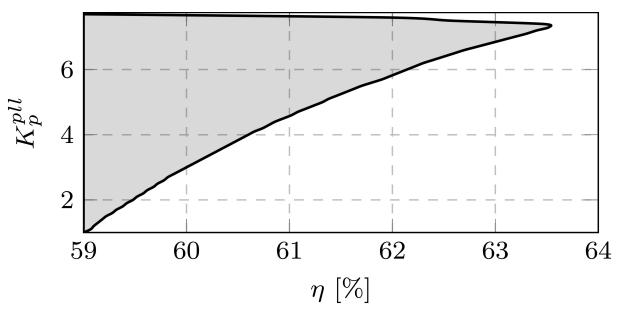

Fig. 15. Stability map in the $K_p^{pll} - \eta$ plane indicating the effect of proportional PLL gain on admissible penetration of *grid-following* inverter units in Scenario III.

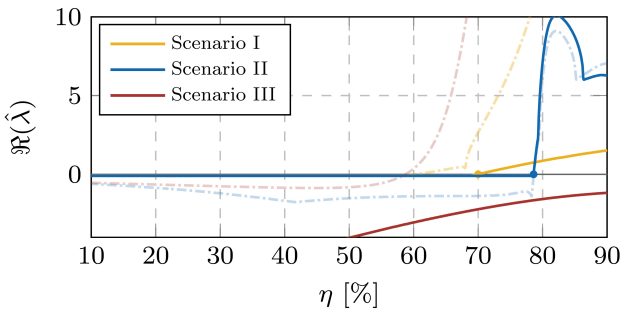

Fig. 16. Impact of inverter penetration on system stability for different unit configuration, with inclusion of transmission line dynamics. Transparent dashed lines indicate results for scenarios without line dynamics from Fig. 10.

0885-8950 (c) 2021 IEEE. Personal use is permitted, but republication/redistribution requires IEEE permission. See http://www.ieee.org/publications_standards/publications/rights/index.html for more information.
Authorized licensed use limited to: Cyprus University of Technology. Downloaded on March 18,2021 at 09:27:38 UTC from IEEE Xplore. Restrictions apply.

However, the line dynamics do not have any impact on the slower modes associated with the synchronous machines. Therefore, the stability in Scenario I cannot be preserved for the *grid-following* penetration above 70 %, as it is associated solely with the AVR and PSS control design. The predominant impact of SGs on system stability is even higher in Scenario II, with *grid-forming* inverters only marginally affecting the critical modes within a narrow range of $\eta \in [78, 79]$ %. Hence, the maximum admissible VSC penetration after the inclusion of transmission line dynamics remains the same in this case.

As a mean of model validation, we investigate the same 2-bus test case comprised only of synchronous generators or *grid-forming* converters. Understandably, networks with such homogeneous configurations of generators with standalone capabilities face no stability problems under any ratio of installed powers between the two units. Therefore, these results are not included in Fig. 16 for simplicity, nor will the respective scenarios be discussed in the remainder of the study.

C. Impact of System Operating Point

In addition to the total installed capacity of PE-interfaced generation, the actual dispatch (i.e., operating power setpoints) of converter-based units can have a detrimental effect on small-signal stability. In fact, it can completely change the nature of the unstable modes and the controllers contributing to such modes and instability. One such example is illustrated in Fig. 17, depicting a root loci spectrum of the system from Scenario II. The SG and *grid-forming* VSC have identical installed power capacities, suggesting that $\eta = 0.5$. Note that for such configuration and $p_g^\star = p_c^\star = 0.5\,\text{p.u.}$, the system in Scenario II is stable (see Fig. 10). The original unit dispatch (set at 50 % for each unit) is modified by gradually changing the power setpoints while holding the total generation output constant, which corresponds to redistribution of the load demand between the two generators.

Under SG-dominated operation the most critical mode (denoted by blue-edged squares in Fig. 17) is associated with voltage control dynamics. This is also identified as the same mode becoming unstable for increased installed VSC capacity, previously pointed out in Section IV-A. However, when increasing the converter dispatch point $p_c^\star$, the aforementioned mode moves to the left-hand side (indicated by the blue arrow), whereas another mode (denoted by red-edged diamonds) shifts to the right-hand side (indicated by the red arrow) and eventually becomes unstable for $p_c^\star > 0.7\,\text{p.u.}$ An interesting observation is that the instability arises from synchronization issues, i.e., it is a consequence of adverse interactions between the two frequency controllers. Such finding confirms a very complex nature of potentially unstable modes in a PE-dominated power system, and implies that a single metric of inverter penetration might not be sufficient to prescribe reliable stability margins. Another insightful remark can be made regarding the nature of the most critical modes, as they all have zero imaginary part. This implies that the underlying instability is not oscillatory, and one should not be thinking of "fast" and "slow" second-order dynamics but rather of just first-order dynamics when referring to these modes.

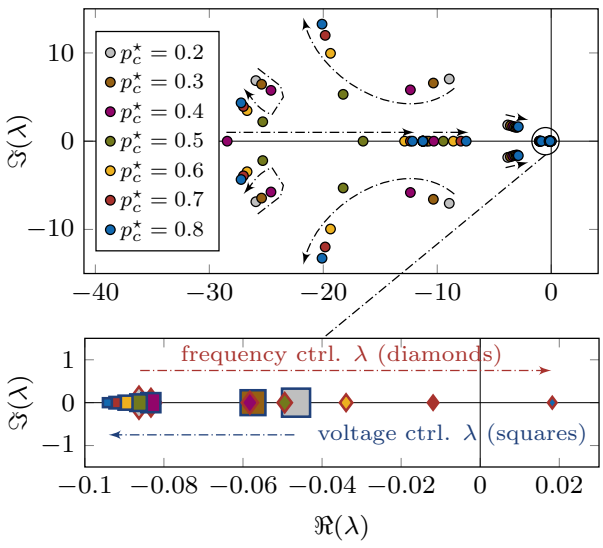

Fig. 17. Root loci spectrum of interest for different system operating points: general mode movement (top) and the most critical modes (bottom). In the bottom figure, the edge color of the mode corresponds to the color of the respective arrow indicating the direction of the movement. The size of the symbol scales down with the increase in converter power setpoint $p_c^\star$.

V. Stability Analyses of Larger Systems

A. Stability Margins of the IEEE 9-bus System

In order to investigate the simultaneous interactions between all three unit types, as well as to increase the network complexity, the IEEE 9-bus system given in Fig. 18 is considered in this case study. A *grid-following* VSC is placed at node 2 and a *grid-forming* VSC at node 3. The transmission line dynamics are included throughout the remainder of the study.

The stability mapping for the IEEE 9-bus system is shown in Fig. 19, considering also different levels of network connectivity. Each triangular axis denotes a penetration of the respective unit type, more precisely η_{SG} refers to synchronous generators, η_F to *grid-forming* and η_f to *grid-following* inverter-based units; colored areas indicate a predominant penetration (≥ 50 %) of a single generation type. It should be noted that the system is always comprised of three generation units, i.e., axes points indicating a 0 % penetration of a single generator type are not considered, and the individual penetration levels are varied in discrete steps of 1 %. We modify the original system by gradually adding transmission lines, first between the generator buses and subsequently between the load buses, as indicated by the red and blue lines in Fig. 18 respectively. Such procedure allows us to increase the network connectivity, defined as

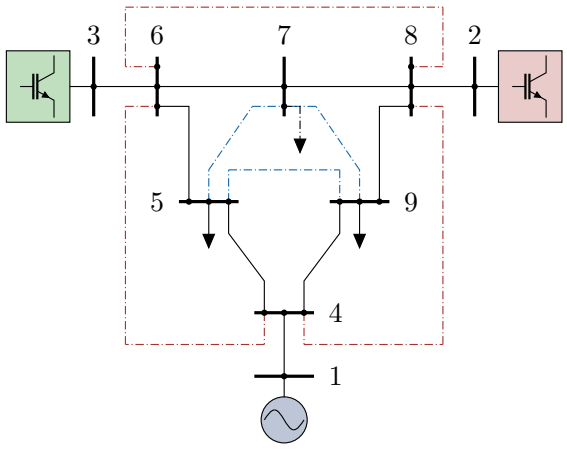

Fig. 18. Network diagram of the IEEE 9-bus system. The blue and red lines indicate the additionally incorporated transmission lines.

0885-8950 (c) 2021 IEEE. Personal use is permitted, but republication/redistribution requires IEEE permission. See http://www.ieee.org/publications_standards/publications/rights/index.html for more information.
Authorized licensed use limited to: Cyprus University of Technology. Downloaded on March 18,2021 at 09:27:38 UTC from IEEE Xplore. Restrictions apply.

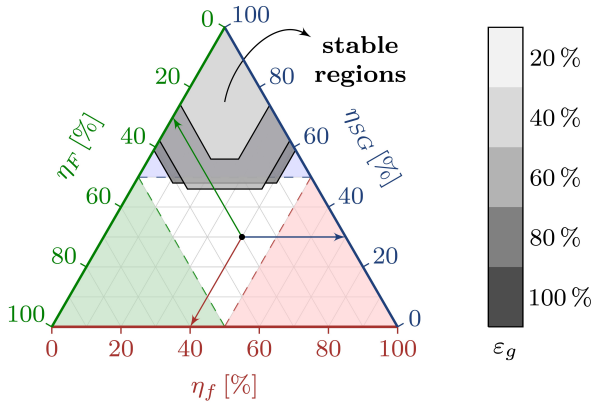

Fig. 19. Stability mapping for the IEEE 9-bus test case under different levels of network connectivity. Colored arrows indicate the appropriate reading direction on the respective axes.

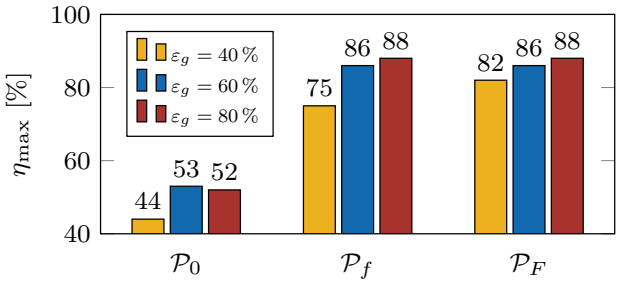

Fig. 20. Maximum permissible inverter penetration under different system portfolios ($\mathcal{P}$) and levels of network connectivity (ε_g).

$\varepsilon_g = 2N_b/(N_n^2 - N_n)$, from $40\,\%$ in the original model to $60\,\%$ and $80\,\%$ in the modified system.

Fig. 19 suggests that, for the generator configuration in this test case, system stability cannot be maintained with less than $47\,\%$ synchronous generation. Reducing connectivity (in particular by removing network connections between generator buses) makes the system even more reliant on synchronous generation. It is clear that stability erodes at high VSC penetration levels independent of the *grid-forming* share, which is consistent with our previous findings in Section IV-A. Interestingly, the permissible converter installation margin significantly reduces when the η_F/η_f ratio diverges from 1, as the maximum value of $\eta = \eta_F + \eta_f$ drops from $44\,\%$ to $27\,\%$ in case of $\eta_F \approx 0\,\%$ or $\eta_f \approx 0\,\%$. This is due to different instabilities occurring between various unit types, specifically voltage issues for a system comprised of synchronous and inverter-based generators (Scenarios I and II) and synchronization obstacles related to a $100\,\%$ PE-based system (Scenario III), as described in Section IV-A. For a rather balanced portfolio, all of these problems are somewhat confined within reasonable limits, while an imbalance in the η_F/η_f ratio tends to emphasize the voltage dynamics issues and endanger the whole network. Another valid point can be made regarding the beneficial impact of transmission line dynamics. As previously indicated in Section IV-B, a direct connection between units experiencing frequency instability mitigates the synchronization issues, thus facilitating a higher share of PE-based devices. Nonetheless, this is not the case for transmission lines between the load nodes, as increasing connectivity from $60\,\%$ to $80\,\%$ has a negligible impact on the stability margin.

We extend this analysis by differentiating between three different generation portfolios: (i) $\mathcal{P}_0$ - a mix of all three unit types, as previously discussed; (ii) $\mathcal{P}_f$ - a system comprised only of synchronous generators and *grid-following* VSCs; and (iii) $\mathcal{P}_F$ - a system comprised only of synchronous generators and *grid-forming* VSCs; in the latter two cases the portfolio consists of two synchronous and one inverter-based generator, i.e., one of the VSCs from the original portfolio $\mathcal{P}_0$ is replaced by SG, whereas the total inverter penetration ratio is equal to either η_f or η_F. The results for the IEEE 9-bus system presented in Fig. 20 suggest that more homogeneous portfolios, such as $\mathcal{P}_f$ and $\mathcal{P}_F$, can withstand drastically higher penetrations of renewables, with $\eta_{\max}$ reaching up to $75\,\%$ and $82\,\%$ respectively. Understandably, portfolio $\mathcal{P}_F$ has a higher η margin due to less accentuated voltage instability compared to the $\mathcal{P}_f$ scenario. However, increasing network connectivity balances these penetration ratios out, as direct transmission line connections resolve the timescale separation between the voltage controllers of synchronous and converter-based generators (see Fig. 9). As a result, the system can facilitate up to $\eta_{\max} = 88\,\%$ of PE-interfaced units; an increase of approximately $70\,\%$ compared to the original portfolio $\mathcal{P}_0$.

Alternatively, a different configuration with a less heterogeneous portfolio comprised of two *grid-forming* and one *grid-following* inverter is investigated. For higher levels of network connectivity the system faces no stability issues under any share of installed powers, whereas in case of $\varepsilon_g = 40\,\%$ the maximum permissible penetration of *grid-following* generation is $93\,\%$. This highlights the fact that the small-signal stability of low-inertia systems is drastically more vulnerable compared to the one of $100\,\%$ PE-based systems.

B. Stability Characteristics of South-East Australian Network

Having gained fundamental understanding of dynamic interactions between different types of generators in a simplistic test environment, we extend the analysis to a 14-generator, 59-bus South-East Australian system [68], [69] shown in Fig. 21. This network represents a long, linear system as opposed to the more tightly meshed networks found in Europe and the United States. For convenience, it has been divided into 5 areas, with areas 1 and 2 being closely electrically coupled. Therefore, there are in essence 4 main regions, namely South Australia (area 5), Queensland (area 4), Victoria (area 3) and New South Wales (subsuming areas 1 and 2), and hence 3 inter-area modes are present. Beside its string topology, the system is characterized by the weak coupling between South Australia and the rest of the system. The model employed in this work considers the light loading scenario provided in [69], [70].

Moreover, for the purpose of this work, the model presented in [70] was modified to obtain a low-inertia case study by replacing synchronous generators located at buses 101, 202, 301, 302, 501, 502 and 503 by *grid-following* VSCs of identical power rating. In addition, we install 4 more *grid-following* units, two in each of the area 2 and 3, at nodes 212 and 214, i.e., 308 and 314 respectively. This yields a total of 11 converter-interfaced generators operating in *grid-following* mode and 7 conventional SGs, representing the default test case for our analysis. Such modeling choice is based on the high penetration of renewable generation in the real-world system, particularly in area 5, that does not provide standalone frequency support [71], [72]. Note that the default test case comprises all-inverter-based areas 5,

0885-8950 (c) 2021 IEEE. Personal use is permitted, but republication/redistribution requires IEEE permission. See http://www.ieee.org/publications_standards/publications/rights/index.html for more information.
Authorized licensed use limited to: Cyprus University of Technology. Downloaded on March 18,2021 at 09:27:38 UTC from IEEE Xplore. Restrictions apply.

This article has been accepted for publication in a future issue of this journal, but has not been fully edited. Content may change prior to final publication. Citation information: DOI 10.1109/TPWRS.2021.3061434, IEEE Transactions on Power Systems

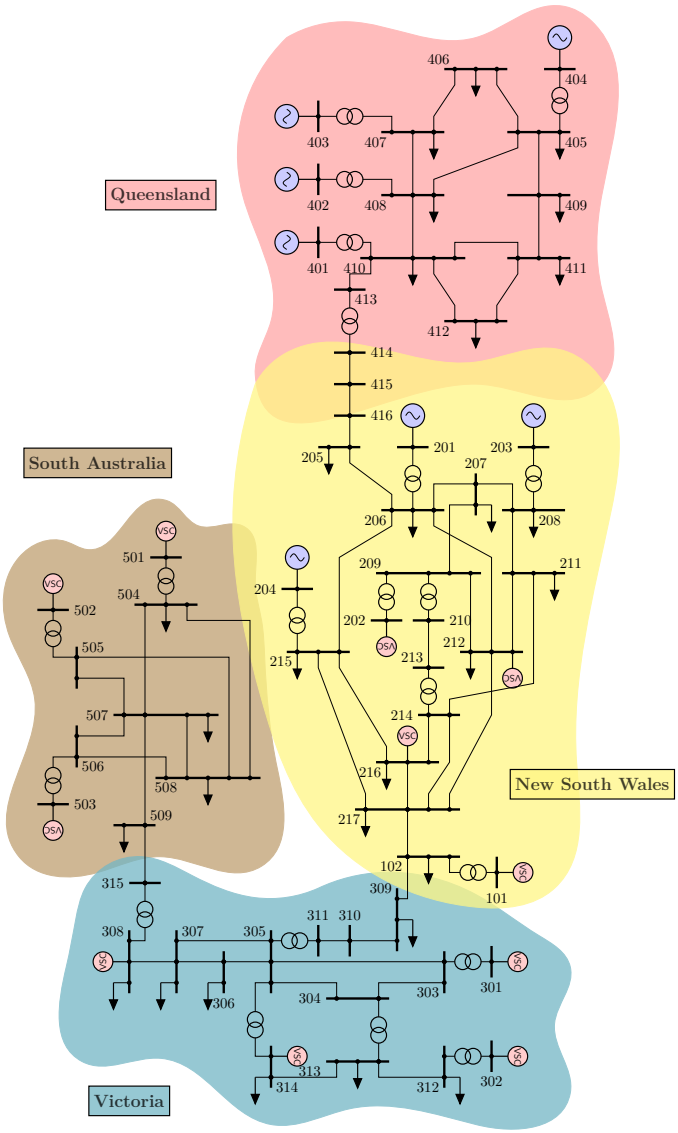

Fig. 21. Modified South-East Australian power system line diagram (default configuration in Scenario 1).

3 and 1, corresponding to South Australia, Victoria and the far south region of New South Wales.

In the following step, we analyze the stability margins of the South-East Australian network for 33 different configuration scenarios categorized into 6 groups, as listed in Fig. 21a. The first set of 8 scenarios ($\mathcal{G}_1$), including the default setup in Scenario 1, is generated by successively replacing one of the existing SGs in Queensland and New South Wales (areas 2 and 4) of the default case by an equivalent *grid-following* inverter. Similarly, set $\mathcal{G}_2$ considers 6 scenarios where two of the aforementioned SGs are simultaneously converted into converter-interfaced units. In contrast, $\mathcal{G}_3$ restores South Australia to its original condition (i.e., makes area 5 SG-based) and presents 9 scenarios with a substantially higher level of inverter penetration in areas 2 and 4, with Scenario 23 only having one SG in Queensland and New South Wales combined. The two scenarios in $\mathcal{G}_4$ are the only instances with *grid-forming* VSC installation and represent 100% inverter-based configurations, whereas sets $\mathcal{G}_5$ and $\mathcal{G}_6$ restore original synchronous generation in areas 1, 3 and 5 and study the impact of PE-based generators in areas 2 and 4. The main distinction between the latter two sets is the substantially higher inverter penetration in the second case.

By closely studying the inverter penetration levels and system configurations[4] in Fig. 21, we can make several insightful observations that validate the claims raised in Section IV and Section V-A. First of all, there is a clear upper bound on the level of *grid-following* inverter penetration that a traditional power system can withstand. For sets $\mathcal{G}_1$ and $\mathcal{G}_2$ this limit corresponds to $\eta_{\max} \in [60-70]$ %, while for $\mathcal{G}_3$, $\mathcal{G}_5$ and $\mathcal{G}_6$ the maximum permissible penetration increases to $\eta_{\max} \in [60-70]$ %. Understandably, the network configuration and unit placement play an important role. This justifies the lower VSC installation margins for former scenarios (sets $\mathcal{G}_1$ and $\mathcal{G}_2$) where South Australia (area 5) is inverter-based, since the electrical distances between the synchronous and inverter-interfaced generation are the longest and hence the system is more vulnerable. We also showcase that the operator should not aim at enforcing a single margin for maximum VSC penetration, as Scenario 22 is stable for $\eta = 78.5\,\%$ while Scenario 2 is unstable for $\eta = 62\,\%$; again, solely due to the outline of the system and placement of the *grid-following* VSCs in the network.

Finally, we validate the notion that an all-inverter network is significantly less prone to instability, as Scenario 24 can withstand a share of $\approx 92\,\%$ *grid-following* inverters while having only two *grid-forming* units in the grid. However, removing one of those *grid-forming* converters leads to frequency instability (Scenario 25). Note that in Scenario 24, the *grid-forming* VSCs are placed at the end nodes of the system (node 501 in South Australia and node 404 in Queensland), thus capable of covering wide areas affected by their "forming" property and facilitating a high *grid-following* inverter penetration. By replacing the *grid-forming* unit at node 404 with a *grid-following* one, the electrical distance between this converter and the *grid-forming* VSC in South Australia becomes too large and the system cannot preserve small-signal stability. We can therefore conclude that the problem of placement of *grid-forming* inverters in a low-inertia system could be of high importance in the future. This topic is addressed in [72]–[74].

VI. Conclusion

The presented paper employs a high-fidelity ODE formulation of a low-inertia system with detailed control schemes of both synchronous and converter-based generators, as well as the dynamics of loads and transmission lines. Using modal analysis techniques we expose the most vulnerable segments of the system under different penetration levels of inverter-based units, various generation portfolios and system operating points, and investigate the adverse effects of the underlying control interference. As a result, some new insights into the overall stability of low- and no-inertia systems are presented, together with the proposed directions for improving the system stability margin under different scenarios and configurations.

The key findings can be summarized as follows: (i) Small-signal stability of low-inertia systems is significantly more vulnerable and harder to ensure compared to $100\,\%$ inverter-based power systems; (ii) Introduction of fast-acting PE devices implies that traditional assumptions of neglecting transmission line dynamics in power system studies might not be valid anymore. Interestingly enough, the line connections could potentially have both positive and adverse effects on system stability,

[4]Synchronous generators are denoted by "S", whereas *grid-forming* and *grid-following* converter-interfaced units are denoted by "F" and "f" respectively.

0885-8950 (c) 2021 IEEE. Personal use is permitted, but republication/redistribution requires IEEE permission. See http://www.ieee.org/publications_standards/publications/rights/index.html for more information.
Authorized licensed use limited to: Cyprus University of Technology. Downloaded on March 18,2021 at 09:27:38 UTC from IEEE Xplore. Restrictions apply.

Scenario		Generation type at the respective node																		η [%]	stable system
		501	502	503	308	314	302	301	101	214	212	204	203	201	401	402	403	404	202		
$\mathcal{G}_1$	1	f	f	f	f	f	f	f	f	f	f	S	S	S	S	S	S	S	f	56.97	yes
	2	f	f	f	f	f	f	f	f	f	f	f	S	S	S	S	S	S	f	61.96	no
	3	f	f	f	f	f	f	f	f	f	f	S	f	S	S	S	S	S	f	66.35	no
	4	f	f	f	f	f	f	f	f	f	f	S	S	f	S	S	S	S	f	64.68	no
	5	f	f	f	f	f	f	f	f	f	f	S	S	S	f	S	S	S	f	63.36	yes
	6	f	f	f	f	f	f	f	f	f	f	S	S	S	S	f	S	S	f	60.83	yes
	7	f	f	f	f	f	f	f	f	f	f	S	S	S	S	S	f	S	f	63.36	yes
	8	f	f	f	f	f	f	f	f	f	f	S	S	S	S	S	S	f	f	61.3	yes
$\mathcal{G}_2$	9	f	f	f	f	f	f	f	f	f	f	S	S	S	S	S	f	f	f	67.68	no
	10	f	f	f	f	f	f	f	f	f	f	S	S	S	S	f	f	S	f	67.21	no
	11	f	f	f	f	f	f	f	f	f	f	S	S	S	f	f	S	S	f	67.21	no
	12	f	f	f	f	f	f	f	f	f	f	S	S	S	S	f	S	f	f	65.16	yes
	13	f	f	f	f	f	f	f	f	f	f	S	S	S	f	S	f	S	f	69.74	yes
	14	f	f	f	f	f	f	f	f	f	f	S	S	S	f	S	S	f	f	67.68	yes
$\mathcal{G}_3$	15	S	S	S	f	f	f	f	f	f	f	f	S	S	S	S	S	f	f	57.98	yes
	16	S	S	S	f	f	f	f	f	f	f	f	f	f	S	S	S	S	f	70.74	no
	17	S	S	S	f	f	f	f	f	f	f	f	f	S	S	S	S	S	f	63.02	yes
	18	S	S	S	f	f	f	f	f	f	f	S	f	f	S	S	S	S	f	65.75	yes
	19	S	S	S	f	f	f	f	f	f	f	f	S	f	S	S	S	S	f	61.36	yes
	20	S	S	S	f	f	f	f	f	f	f	f	S	f	S	S	S	f	f	65.69	yes
	21	S	S	S	f	f	f	f	f	f	f	f	S	f	f	S	S	f	f	72.07	yes
	22	S	S	S	f	f	f	f	f	f	f	f	S	f	f	S	f	f	f	78.45	yes
	23	S	S	S	f	f	f	f	f	f	f	f	S	f	f	f	f	f	f	82.31	no
$\mathcal{G}_4$	24	F	f	f	f	f	f	f	f	f	f	f	f	f	f	f	f	F	f	91.95	yes
	25	F	f	f	f	f	f	f	f	f	f	f	f	f	f	f	f	f	f	96.27	no
$\mathcal{G}_5$	26	S	S	S	f	f	S	S	S	f	f	S	S	S	S	S	S	S	S	22.47	yes
	27	S	S	S	f	f	S	S	S	f	f	f	S	S	S	S	S	S	S	27.45	yes
	28	S	S	S	f	f	S	S	S	f	f	S	f	S	S	S	S	S	S	31.84	yes
$\mathcal{G}_6$	29	S	S	S	f	f	S	S	S	f	f	S	f	f	S	f	f	S	f	58.97	yes
	30	S	S	S	f	f	S	S	S	f	f	f	f	f	S	f	f	S	f	63.95	yes
	31	S	S	S	f	f	S	S	S	f	f	f	f	f	S	f	f	f	f	68.28	yes
	32	S	S	S	f	f	S	S	S	f	f	f	f	f	f	f	f	f	f	74.66	no
	33	S	S	S	f	f	S	S	S	f	f	f	f	f	f	f	f	S	f	70.34	yes

Fig. 22. Scenario configuration and stability analysis of South-East Australian grid based on the generation portfolio in the system.

depending on the generation portfolio; (iii) Contrary to popular belief, low inertia on its own does not have a major impact on the small-signal stability of power systems with high shares of PE-interfaced generation. It does however affect frequency dynamics and associated fast transients, which in turn can adversely trigger numerous protection schemes based on Rate-of-Change-of-Frequency (RoCoF) measurements; (iv) Controllers of synchronous and inverter-based generators can interact in a way that leads to frequency and voltage instabilities under high penetration of renewables. This can only be observed under sufficiently detailed modeling of underlying control schemes; (v) In addition to installed inverter capacity, the operating points have a crucial impact on overall stability and can drastically change the nature of unstable modes and underlying dynamics, which in turn could affect the optimal power flow dispatch.

Future research could include, among other things, a comprehensive analysis of potentially adverse effects of incompatible converter control strategies, impact of unit placement on transient and small-signal stability, as well as the overall system capability for frequency regulation (e.g., limiting nadir and RoCoF) under high inverter penetration. Furthermore, the aspects of large-signal stability and the impact of HVDC and MTDC grids should be thoroughly investigated.

REFERENCES

[1] F. Milano, F. Dörfler, G. Hug, D. J. Hill, and G. Verbič, "Foundations and challenges of low-inertia systems," in *Power Systems Computation Conference (PSCC)*, Jun 2018.

[2] P. Kundur, *Power System Stability and Control*. McGraw-Hill, 1994.

[3] J. Machowski, J. W. Bialek, and J. R. Bumby, *Power System Dynamics: Stability and Control*. Wiley, 2008.

[4] D. Mondal, A. Chakrabarti, and A. Sengupta, *Power System Small Signal Stability Analysis and Control*. Elsevier - Academic Press, 2014.

[5] S. D'Arco, J. A. Suul, and O. B. Fosso, "Small-signal modelling and parametric sensitivity of a virtual synchronous machine," in *Power Systems Computation Conference*, Aug 2014.

[6] O. Mo, S. D'Arco, and J. A. Suul, "Evaluation of virtual synchronous machines with dynamic or quasi-stationary machine models," *IEEE Trans. Ind. Electron.*, vol. 64, no. 7, pp. 5952–5962, July 2017.

[7] G. S. Misyris, J. A. Mermet-Guyennet, S. Chatzivasileiadis, and T. Weckesser, "Grid supporting vscs in power systems with varying inertia and short-circuit capacity," in *2019 IEEE Milan PowerTech*, June 2019.

[8] R. Ofir, U. Markovic, P. Aristidou, and G.Hug, "Droop vs. virtual inertia: Comparison from the perspective of converter operation mode," in *IEEE International Energy Conference (ENERGYCON)*, June 2018.

[9] U. Markovic, J. Vorwerk, P. Aristidou, and G. Hug, "Stability analysis of converter control modes in low-inertia power systems," in *IEEE Innovative Smart Grid Technologies Conference Europe*, Oct 2018.

[10] U. Markovic, O. Stanojev, P. Aristidou, and G. Hug, "Partial grid forming concept for 100% inverter-based transmission systems," in *IEEE PES General Meeting*, Aug 2018.

[11] E. A. A. Coelho, P. C. Cortizo, and P. F. D. Garcia, "Small-signal stability for parallel-connected inverters in stand-alone ac supply systems," *IEEE Trans. Ind. Appl.*, vol. 38, no. 2, pp. 533–542, March 2002.

[12] S. V. Iyer, M. N. Belur, and M. C. Chandorkar, "A generalized computational method to determine stability of a multi-inverter microgrid," *IEEE Trans. Power Electron.*, vol. 25, no. 9, pp. 2420–2432, Sep. 2010.

[13] X. Guo, Z. Lu, B. Wang, X. Sun, L. Wang, and J. M. Guerrero, "Dynamic phasors-based modeling and stability analysis of droop-controlled inverters for microgrid applications," *IEEE Trans. Smart Grid*, vol. 5, no. 6, pp. 2980–2987, Nov 2014.

[14] S. D'Arco and J. A. Suul, "Small-signal analysis of an isolated power system controlled by a virtual synchronous machine," in *IEEE International Power Electronics and Motion Control Conference*, Sep. 2016.

[15] J. W. Simpson-Porco, F. Drfler, and F. Bullo, "Synchronization and power sharing for droop-controlled inverters in islanded microgrids," *Automatica*, vol. 49, no. 9, pp. 2603 – 2611, 2013.

[16] J. W. Simpson-Porco, F. Dörfler, and F. Bullo, "Voltage stabilization in microgrids via quadratic droop control," *52nd IEEE Conference on Decision and Control*, 2013.

0885-8950 (c) 2021 IEEE. Personal use is permitted, but republication/redistribution requires IEEE permission. See http://www.ieee.org/publications_standards/publications/rights/index.html for more information.
Authorized licensed use limited to: Cyprus University of Technology. Downloaded on March 18,2021 at 09:27:38 UTC from IEEE Xplore. Restrictions apply.

This article has been accepted for publication in a future issue of this journal, but has not been fully edited. Content may change prior to final publication. Citation information: DOI 10.1109/TPWRS.2021.3061434, IEEE Transactions on Power Systems

[17] J. Schiffer, R. Ortega, A. Astolfi, J. Raisch, and T. Sezi, "Conditions for stability of droop-controlled inverter-based microgrids," *Automatica*, vol. 50, no. 10, pp. 2457 – 2469, 2014.

[18] N. Pogaku, M. Prodanovic, and T. C. Green, "Modeling, analysis and testing of autonomous operation of an inverter-based microgrid," *IEEE Trans. Power Electron.*, vol. 22, no. 2, pp. 613–625, 2007.

[19] G. Diaz, C. Gonzalez-Moran, J. Gomez-Aleixandre, and A. Diez, "Complex-valued state matrices for simple representation of large autonomous microgrids supplied by pq and vf generation," *IEEE Trans. Power Syst.*, vol. 24, no. 4, pp. 1720–1730, Nov 2009.

[20] S. Leitner, M. Yazdanian, A. Mehrizi-Sani, and A. Muetze, "Small-signal stability analysis of an inverter-based microgrid with internal model-based controllers," *IEEE Trans. Smart Grid*, vol. 9, no. 5, pp. 5393–5402, Sep. 2018.

[21] I. P. Nikolakakos, H. H. Zeineldin, M. S. El-Moursi, and N. D. Hatziargyriou, "Stability evaluation of interconnected multi-inverter microgrids through critical clusters," *IEEE Trans. Power Syst.*, vol. 31, no. 4, pp. 3060–3072, July 2016.

[22] N. Pogaku, M. Prodanovic, and T. C. Green, "Modeling, analysis and testing of autonomous operation of an inverter-based microgrid," *IEEE Trans. Power Electron.*, vol. 22, no. 2, pp. 613–625, March 2007.

[23] Q. Peng, Q. Jiang, Y. Yang, T. Liu, H. Wang, and F. Blaabjerg, "On the stability of power electronics-dominated systems: Challenges and potential solutions," *IEEE Trans. Ind. Appl.*, pp. 1–1, 2019.

[24] M. Zhao, X. Yuan, J. Hu, and Y. Yan, "Voltage dynamics of current control time-scale in a vsc-connected weak grid," *IEEE Trans. Power Syst.*, vol. 31, no. 4, pp. 2925–2937, July 2016.

[25] H. Yuan, X. Yuan, and J. Hu, "Modeling of grid-connected vscs for power system small-signal stability analysis in dc-link voltage control timescale," *IEEE Trans. Power Syst.*, vol. 32, no. 5, pp. 3981–3991, Sep. 2017.

[26] EirGrid and SONI, "DS3: System services review TSO recommendations," EirGrid, Tech. Rep., May 2013.

[27] J. Matevosyan and P. Du, "Wind integration in ERCOT," in *Integration of Large-Scale Renewable Energy into Bulk Power Systems*. Springer, 2017.

[28] Australian Energy Market Operator, "Black System South Australia 28 September 2016 - Final Report," Tech. Rep., March 2017.

[29] "PSLF", GE Energy Consulting. [Online]. Available: http://www.geenergyconsulting.com/practice-area/software-products/pslf

[30] "TSAT", Powertech Labs Inc. [Online]. Available: https://www.dsatools.com/tsat/

[31] "PSS®E", Siemens PTI. [Online]. Available: https://new.siemens.com/global/en/products/energy/services/transmission-distribution-smart-grid/consulting-and-planning/pss-software/pss-e.html

[32] P. Pourbeik, J. J. Sanchez-Gasca, J. Senthil, J. D. Weber, P. S. Zadehkhost, Y. Kazachkov, S. Tacke, J. Wen, and A. Ellis, "Generic dynamic models for modeling wind power plants and other renewable technologies in large-scale power system studies," *IEEE Trans. Energy Convers.*, vol. 32, no. 3, pp. 1108–1116, Sep. 2017.

[33] J. Slootweg and W. Kling, "The impact of large scale wind power generation on power system oscillations," *Electric Power Systems Research*, vol. 67, no. 1, pp. 9 – 20, 2003.

[34] A. Mendonca and J. A. P. Lopes, "Impact of large scale wind power integration on small signal stability," in *2005 International Conference on Future Power Systems*, Nov 2005.

[35] D. Gautam, V. Vittal, and T. Harbour, "Impact of increased penetration of dfig-based wind turbine generators on transient and small signal stability of power systems," *IEEE Trans. Power Syst.*, vol. 24, no. 3, pp. 1426–1434, Aug 2009.

[36] P. N. Papadopoulos and J. V. Milanovi, "Probabilistic framework for transient stability assessment of power systems with high penetration of renewable generation," *IEEE Trans. Power Syst.*, vol. 32, no. 4, pp. 3078–3088, July 2017.

[37] X. Xi, H. Geng, and G. Yang, "Small signal stability of weak power system integrated with inertia tuned large scale wind farm," in *2014 IEEE Innovative Smart Grid Technologies - Asia (ISGT ASIA)*, May 2014.

[38] R. Elliott, R. Byrne, A. Ellis, and L. Grant, "Impact of increased photovoltaic generation on inter-area oscillations in the western north american power system," in *2014 IEEE PES General Meeting*, July 2014.

[39] F. Katiraei, M. R. Iravani, and P. W. Lehn, "Small-signal dynamic model of a micro-grid including conventional and electronically interfaced distributed resources," *IET Generation, Transmission Distribution*, vol. 1, no. 3, pp. 369–378, May 2007.

[40] Y. Lin, B. Johnson, V. Gevorgian, V. Purba, and S. Dhople, "Stability assessment of a system comprising a single machine and inverter with scalable ratings," in *North American Power Symposium*, Sep. 2017.

[41] P. W. Sauer and M. A. Pai, *Power system dynamics and stability*. Prentice Hall, 1997.

[42] G. Pinares, "Analysis of the dc dynamics of vsc-hvdc systems connected to weak ac grids using a frequency domain approach," in *2014 Power Systems Computation Conference*, Aug 2014.

[43] M. C. Chandorkar, D. M. Divan, and R. Adapa, "Control of parallel connected inverters in standalone AC supply systems," vol. 29, no. 1, pp. 136–143, 1993.

[44] J. W. Simpson-Porco, F. Dörfler, and F. Bullo, "Synchronization and power sharing for droop-controlled inverters in islanded microgrids," *Automatica*, vol. 49, no. 9, pp. 2603–2611, 2013.

[45] H. P. Beck and R. Hesse, "Virtual synchronous machine," in *2007 9th International Conference on Electrical Power Quality and Utilisation*, Oct 2007.

[46] S. D'Arco, J. A. Suul, and O. B. Fosso, "Virtual synchronous machines - classification of implementations and analysis of equivalence to droop controllers for microgrids," in *2013 IEEE Grenoble Conference*, June 2013.

[47] M. Colombino, D. Groß, J.-S. Brouillon, and F. Dörfler, "Global phase and magnitude synchronization of coupled oscillators with application to the control of grid-forming power inverters," 2019.

[48] D. Groß, M. Colombino, J.-S. Brouillon, and F. Dörfler, "The effect of transmission-line dynamics on grid-forming dispatchable virtual oscillator control," 2019.

[49] T. Jouini, C. Arghir, and F. Dörfler, "Grid-friendly matching of synchronous machines by tapping into the DC storage," in *IFAC Workshop on Distributed Estimation and Control in Networked Systems (NecSys*, 2016, pp. 192–197.

[50] C. Arghir, T. Jouini, and F. Dörfler, "Grid-forming control for power converters based on matching of synchronous machines," *Automatica*, vol. 95, pp. 273 – 282, 2018.

[51] S.-K. Chung, "A phase tracking system for three phase utility interface inverters," *IEEE Trans. Power Electron.*, vol. 15, no. 3, pp. 431–438, May 2000.

[52] S. F. Zarei, H. Mokhtari, M. A. Ghasemi, S. Peyghami, P. Davari, and F. Blaabjerg, "Control of grid-following inverters under unbalanced grid conditions," *IEEE Trans. Energy Convers.*, pp. 1–1, 2019.

[53] M. C. Chandorkar, D. M. Divan, and R. Adapa, "Control of parallel connected inverters in standalone ac supply systems," *IEEE Trans. Ind. Appl.*, vol. 29, no. 1, pp. 136–143, Jan. 1993.

[54] V. Mariani, F. Vasca, J. C. Vsquez, and J. M. Guerrero, "Model order reductions for stability analysis of islanded microgrids with droop control," *IEEE Trans. Ind. Electron.*, vol. 62, no. 7, pp. 4344–4354, July 2015.

[55] J. W. Simpson-Porco, F. Drfler, and F. Bullo, "Voltage stabilization in microgrids via quadratic droop control," *IEEE Trans. Autom. Control*, vol. 62, no. 3, pp. 1239–1253, March 2017.

[56] T. Qoria, F. Gruson, F. Colas, X. Guillaud, M. Debry, and T. Prevost, "Tuning of cascaded controllers for robust grid-forming voltage source converter," in *Power Systems Computation Conference*, 2018.

[57] T. Qoria, U. Markovic, T. Jouini, D. Groß, G. Denis, and T. Prevost, "Data underlying the research of a 3 bus model for full inverter system - Migrate WP3," 2018. [Online]. Available: https://doi.org/10.4121/uuid:e5497fd2-f617-4573-b6d5-1202ebae411d

[58] ENTSO-E, "Documentation on controller tests in test grid configurations," Tech. Rep., November 2013.

[59] J. M. Uudrill, "Dynamic stability calculations for an arbitrary number of interconnected synchronous machines," *IEEE Trans. Power Apparatus and Systems*, vol. PAS-87, no. 3, pp. 835–844, March 1968.

[60] C. Spanias and I. Lestas, "A system reference frame approach for stability analysis and control of power grids," *ArXiv e-prints*, Sep. 2018.

[61] P. M. Anderson and A. A. Fouad, *Power system control and stability*. John Wiley & Sons, 2008.

[62] E. Ekomwenrenren, H. Alharbi, T. Elgorashi, J. Elmirghani, and P. Aristidou, "Stabilising control strategy for cyber-physical power systems," *IET Cyber-Physical Systems: Theory Applications*, vol. 4, no. 3, pp. 265–275, 2019.

[63] P. Kundur, J. Paserba, V. Ajjarapu, G. Andersson, A. Bose, C. Canizares, N. Hatziargyriou, D. Hill, A. Stankovic, C. Taylor, T. Van Cutsem, and V. Vittal, "Definition and classification of power system stability IEEE/CIGRE joint task force on stability terms and definitions," *IEEE Trans. Power Syst.*, vol. 19, no. 3, pp. 1387–1401, Aug 2004.

[64] P. Vorobev, P. Huang, M. A. Hosani, J. L. Kirtley, and K. Turitsyn, "A framework for development of universal rules for microgrids stability and control," in *IEEE 56th Conference on Decision and Control*, Dec 2017.

[65] D. Groß, M. Colombino, J.-S. Brouillon, and F. Dörfler, "The effect of transmission-line dynamics on grid-forming dispatchable virtual oscillator control," *ArXiv e-prints*, Feb. 2018.

[66] P. Vorobev, P. Huang, M. A. Hosani, J. L. Kirtley, and K. Turitsyn, "High-fidelity model order reduction for microgrids stability assessment," *IEEE Trans. Power Syst.*, vol. 33, no. 1, pp. 874–887, Jan 2018.

[67] W. Du, R. H. Lasseter, and A. S. Khalsa, "Survivability of autonomous microgrid during overload events," *IEEE Trans. Smart Grid*, Apr 2018.

[68] A. S. Ahmadyar, S. Riaz, G. Verbi, A. Chapman, and D. J. Hill, "A framework for assessing renewable integration limits with respect to frequency performance," *IEEE Trans. Power Syst.*, vol. 33, no. 4, 2018.

[69] M. J. Gibbard and D. J. Vowles, "Simplified 14-generator model of the se australian power system," 2010.

[70] A. Moeini, I. Kamwa, P. Brunelle, and G. Sybille, "Open data ieee test systems implemented in simpowersystems for education and research in power grid dynamics and control," in *2015 50th International Universities Power Engineering Conference (UPEC)*, Sep. 2015.

0885-8950 (c) 2021 IEEE. Personal use is permitted, but republication/redistribution requires IEEE permission. See http://www.ieee.org/publications_standards/publications/rights/index.html for more information.
Authorized licensed use limited to: Cyprus University of Technology. Downloaded on March 18,2021 at 09:27:38 UTC from IEEE Xplore. Restrictions apply.

This article has been accepted for publication in a future issue of this journal, but has not been fully edited. Content may change prior to final publication. Citation information: DOI 10.1109/TPWRS.2021.3061434, IEEE Transactions on Power Systems

[71] S. Püschel-Løvengreen and P. Mancarella, "Frequency response constrained economic dispatch with consideration of generation contingency size," in *2018 Power Systems Computation Conference (PSCC)*, June 2018.
[72] B. Kameshwar Poolla, D. Groß, and F. Dörfler, "Placement and implementation of grid-forming and grid-following virtual inertia," *IEEE Trans. Power Syst.*, vol. 34, no. 4, pp. 3035–3046, 2019.
[73] D. Groß, S. Bolognani, B. Poolla, and F. Dörfler, "Increasing the resilience of low-inertia power systems by virtual inertia and damping," in *IREP Bulk Power System Dynamics & Control Symposium*, Aug 2017.
[74] A. Venkatraman, U. Markovic, D. Shchetinin, E. Vrettos, P. Aristidou, and G. Hug, "Improving Dynamic Properties of Low-Inertia Systems through Eigensensitivity Optimization," *IEEE Trans. Power Syst.*, vol. 36, no. 3, pp. 1–14, 2021.

APPENDIX

A. Vector Formulation of Circuit Dynamics

We derive the dq-vector formulation for a general RL circuit described by the per-unit series resistance $r \in \mathbb{R}_{>0}$ and inductance $\ell \in \mathbb{R}_{>0}$. Let us consider such series impedance, with three-phase voltages $v_1^{abc} \in \mathbb{R}^3$ and $v_2^{abc} \in \mathbb{R}^3$ at the respective ends and the three-phase current $i^{abc} \in \mathbb{R}^3$ flowing through it. Assuming a base angular velocity $\omega_b \in \mathbb{R}_{>0}$, the current dynamics are described in per-unit by

$$\tfrac{\mathrm{d}}{\mathrm{d}t} i^{abc} = -\frac{\omega_b}{\ell}\left(v_1^{abc} - v_2^{abc}\right) - \frac{r}{\ell}\omega_b i^{abc}, \tag{30}$$

Moreover, let us denote by $X(\theta_r) = T(\theta_r)^{-1}$ the inverse of the power-variant dq-transform in (3). Assuming a balanced three-phase system and, given a reference angle $\theta_r \in [-\pi, \pi)$ of the dq-frame, expression (30) can be rewritten as

$$\tfrac{\mathrm{d}}{\mathrm{d}t}\left(X i^{dq}\right) = -\frac{\omega_b}{\ell} X\left(v_1^{dq} - v_2^{dq}\right) - \frac{r}{\ell}\omega_b X i^{dq}. \tag{31}$$

Considering that $\frac{\mathrm{d}}{\mathrm{d}t}\theta_r = \omega_b\omega_r$ and that $j := \mathcal{R}(\pi/2)$ can be interpreted as an embedding of the complex imaginary unit $\sqrt{-1}$ into $\mathbb{R}^2$, the term on the left-hand side of (31) can be further expressed as

$$\tfrac{\mathrm{d}}{\mathrm{d}t}\left(X i^{dq}\right) = \tfrac{\mathrm{d}}{\mathrm{d}t}\left(X\right) i^{dq} + X\tfrac{\mathrm{d}}{\mathrm{d}t} i^{dq} = j\omega_b\omega_r i^{dq} + X\tfrac{\mathrm{d}}{\mathrm{d}t}\left(i^{dq}\right). \tag{32}$$

Substituting (32) into (31) and conducting a set of trivial mathematical operations yields

$$\tfrac{\mathrm{d}}{\mathrm{d}t} i^{dq} = \frac{\omega_b}{\ell}\left(v_1^{dq} - v_2^{dq}\right) - \left(\frac{r}{\ell}\omega_b + j\omega_b\omega_r\right) i^{dq}. \tag{33}$$

B. Frequency Control Loop of a Grid-Forming Converter in a Multi-Machine System

Let us consider an index set $\mathcal{N}_g$ representing all interconnected *grid-forming* converters with the droop-based active power control (10) described by

$$\tau_z \dot{\omega}_{c_j} = \omega_{c_j}^\star - \omega_{c_j} + R_c^p\left(p_{c_j}^\star - p_{c_j}\right), \forall j \in \mathcal{N}_g, \tag{34}$$

where $\tau_z = \omega_z^{-1}$ is the time constant of the low-pass filter. Having in mind that $\dot{\theta}_{c_j} = \omega_b\omega_{c_j}$, one can transform (34) into

$$\tau_z \ddot{\theta}_{c_j} = -\dot{\theta}_{c_j} + \omega_b\omega_{c_j}^\star + \omega_b R_c^p\left(p_{c_k}^\star - p_{c_k}\right). \tag{35}$$

The converter's output power p_{c_j} can be described as the sum of all powers flowing across the transmission lines connecting VSC j to the adjacent converter units $k \in \mathcal{K}_j$:

$$p_{c_j} = \sum_{k\in\mathcal{K}_j} p_{jk} = \sum_{k\in\mathcal{K}_j} v_{c_j}^\mathsf{T} i_{jk}, \tag{36}$$

with $v_{c_j} := v_{f_j}$ corresponding to the filter output voltage of the respective converter $j \in \mathcal{N}_g$, i_{jk} being the vector of the current flowing through the line between converters j and k, and $\theta_{jk} := \theta_{c_j} - \theta_{c_k}$ Furthermore, considering line parameters of the form $(r_{jk}, \ell_{jk}) \in \mathbb{R}_{>0}$, we express the electromagnetic dynamics of the line current in a dq-frame by (see Appendix A)

$$\dot{i}_{jk} = \frac{\omega_b}{\ell_{jk}}(v_{c_j} - v_{c_k}) - \left(\frac{r_{jk}}{\ell_{jk}}\omega_b + j\omega_b\omega_0\right) i_{jk}, \tag{37}$$

which is subsequently transformed into frequency (Laplace) domain as

$$i_{jk} = \frac{v_{c_j} - v_{c_k}}{r_{jk} + j\omega_0\ell_{jk} + s\ell_{jk}/\omega_b}. \tag{38}$$

Let us define $i_{jk}^0 \in \mathbb{R}^2$ as the nominal current flowing through the line (r_{jk}, ℓ_{jk}) with the end voltages $v_{c_j} \in \mathbb{R}^2$ and $v_{c_k} \in \mathbb{R}^2$, i.e.,

$$i_{jk}^0 = \frac{v_{c_j} - v_{c_k}}{r_{jk} + j\omega_0\ell_{jk}}. \tag{39}$$

Substituting (39) into (38) yields

$$i_{jk} = \frac{i_{jk}^0}{1 + \underbrace{s\ell_{jk}/\left(r_{jk} + j\omega_0\ell_{jk}\right)\omega_b}_{\sigma_l}}. \tag{40}$$

Note that σ_l can be expressed using SI terms as

$$\sigma_l = \frac{s\ell_{jk}}{\left(r_{jk} + j\omega_0\ell_{jk}\right)\omega_b} = \frac{sL_{jk}}{R_{jk} + j\omega_0 L_{jk}} = \frac{sT_{jk}}{1 + j\omega_0 T_{jk}}, \tag{41}$$

with $T_{jk} = \frac{L_{jk}}{R_{jk}}$ being the transmission line time constant. Considering that $\frac{X_l}{R_{jk}} \approx 10$, we can assume $T_{jk} \approx 0.03\,\mathrm{s}$. Therefore, it is reasonable to assume that $\sigma_l \ll 1$ holds for modes evolving on the timescales shorter than the line time constant T_{jk} [66]. By performing a first-order Taylor series expansion $(1+\sigma_l)^{-1} \approx 1 - \sigma_l$, we can rewrite (40) as

$$i_{jk} \approx i_{jk}^0 - \frac{s\ell_{jk}}{\omega_b\left(r_{jk} + j\omega_0\ell_{jk}\right)} i_{jk}^0, \tag{42}$$

and transform it back into the time-domain form

$$i_{jk} \approx i_{jk}^0 - \frac{\ell_{jk}}{\omega_b\left(r_{jk} + j\omega_0\ell_{jk}\right)^2}\left(\dot{v}_{c_j} - \dot{v}_{c_k}\right). \tag{43}$$

Assuming nominal voltage magnitudes and small angle deviations between the nodes, i.e., $\|v_{c_j}\| \approx 1\,\mathrm{p.u.}$ and $\theta_{jk} \approx 0, \forall j \in \mathcal{N}_g, \forall k \in \mathcal{K}_j$, we can compute the time derivatives of voltage vectors and subsequently the total active power injection as

$$\begin{aligned} p_{c_j} &= \sum_{k\in\mathcal{K}_j}\left(\frac{\omega_0\ell_{jk}}{\omega_b\left(r_{jk}^2 + \omega_0^2\ell_{jk}^2\right)^2}\theta_{c_j} + \frac{2r_{jk}\ell_{jk}^2}{\omega_b\left(r_{jk}^2 + \omega_0^2\ell_{jk}^2\right)^2}\dot{\theta}_{c_j}\right) \\ &= B_j\theta_{c_j} + B_j'\dot{\theta}_{c_j}. \end{aligned} \tag{44}$$

Substituting (44) into (34) yields the frequency dynamics of an individual inverter of the form

$$\tau_z\ddot{\theta}_{c_j} + \left(1 - \omega_b R_c^p B_j'\right)\dot{\theta}_{c_j} + \omega_b R_c^p B_j\theta_{c_j} + C_j = 0, \tag{45}$$

with $C_j = \omega_b\omega_{c_j}^\star + \omega_b R_c^p p_{c_j}^\star$.

0885-8950 (c) 2021 IEEE. Personal use is permitted, but republication/redistribution requires IEEE permission. See http://www.ieee.org/publications_standards/publications/rights/index.html for more information.
Authorized licensed use limited to: Cyprus University of Technology. Downloaded on March 18,2021 at 09:27:38 UTC from IEEE Xplore. Restrictions apply.

This article has been accepted for publication in a future issue of this journal, but has not been fully edited. Content may change prior to final publication. Citation information: DOI 10.1109/TPWRS.2021.3061434, IEEE Transactions on Power Systems

Uros Markovic (S'16-M'20) was born in Belgrade, Serbia. He received the Dipl.-Eng. degree in Electrical Engineering from the University of Belgrade, Serbia, in 2013, with a major in power systems. He obtained the M.Sc. and Ph.D. degrees in Electrical Engineering and Information Technology in 2016 and 2020, respectively, both from the Swiss Federal Institute of Technology (ETH), Zurich, Switzerland. He is currently a joint Postdoctoral researcher with the Power Systems Laboratory and the Automatic Control Laboratory of ETH Zurich, Switzerland, and an affiliated researcher at the Grid Integration Group (GIG) of Lawrence Berkeley National Laboratory (LBNL), California, USA.

His research interests include power system dynamics, control and optimization, with a focus on stability and operation of inverter-dominated power systems with low rotational inertia.

Ognjen Stanojev (S'18) received the B.Sc. degree in Electrical and Computer Engineering with a major in power systems from the University of Novi Sad, Serbia, in 2017. He obtained the M.Sc. degree in Electrical Engineering and Information Technology in 2019 from the Swiss Federal Institute of Technology, Zurich, Switzerland, where he is currently working towards the Ph.D. degree in the Power Systems Laboratory (PSL) since October 2019. His research interests include control and optimization of low inertia power systems.

Petros Aristidou (S'10-M'15-SM'20) received a Diploma in Electrical and Computer Engineering from the National Technical University of Athens, Greece, in 2010, and a Ph.D. in Engineering Sciences from the University of Liège, Belgium, in 2015. He is currently a Lecturer in Sustainable Power Systems at the Cyprus University of Technology. His research interests include power system dynamics, control, and simulation.

Evangelos Vrettos (S'09-M'17) received the Dipl.-Ing degree in Electrical and Computer Engineering from the National Technical University of Athens, Greece, in 2010, with a major in power systems. He joined the Power Systems Laboratory (PSL) at the Swiss Federal Institute of Technology (ETH), Zurich, Switzerland, in 2011, where he obtained the Ph.D. degree in Electrical Engineering and Information Technology in 2016, and continued as a Postdoctoral researcher for half a year. He is currently an R&D Manager at Swissgrid, the Swiss electricity transmission system operator, and an affiliated researcher at the Grid Integration Group (GIG) of Lawrence Berkeley National Laboratory (LBNL), California, USA.

His research has focused on optimization and control for demand response and energy storage resources, low-inertia power systems and, more recently, optimal power flow applications for congestion management and blockchain-based solutions for ancillary services markets.

Duncan Callaway (M'08) is an Associate Professor of Energy and Resources at the University of California, Berkeley. He is also a faculty affiliate in Electrical Engineering and Computer Science, and a faculty scientist at Lawrence Berkeley Laboratory. He received his PhD from Cornell University. He has held engineering positions at Davis Energy Group and PowerLight Corporation, and academic positions at UC Davis, the University of Michigan and UC Berkeley. Duncan teaches courses on electric power systems and at the intersection of statistical learning and energy. His research focuses on grid integration of renewable electricity and models and control strategies for demand response, electric vehicles and electricity storage.

Gabriela Hug (S'05-M'08-SM'14) was born in Baden, Switzerland. She received the M.Sc. degree in electrical engineering in 2004 and the Ph.D. degree in 2008, both from the Swiss Federal Institute of Technology (ETH), Zurich, Switzerland. After the Ph.D. degree, she worked in the Special Studies Group of Hydro One, Toronto, ON, Canada, and from 2009 to 2015, she was an Assistant Professor in Carnegie Mellon University, Pittsburgh, PA, USA. She is currently an Associate Professor in the Power Systems Laboratory, ETH Zurich. Her research is dedicated to control and optimization of electric power systems.

0885-8950 (c) 2021 IEEE. Personal use is permitted, but republication/redistribution requires IEEE permission. See http://www.ieee.org/publications_standards/publications/rights/index.html for more information.
Authorized licensed use limited to: Cyprus University of Technology. Downloaded on March 18,2021 at 09:27:38 UTC from IEEE Xplore. Restrictions apply.